Response to reviewer#2

Thanks for the reviewer's helpful suggestions! The comments are addressed point-by-point and responses are listed below.

Comment: *This paper reports a method combing a DMA with an aethalometer to obtain the BC mass size distribution (BCMSD). Two modes of the BCMSD are observed in their ambient measurement in the North China Plain with the new method. Also, they found that the BCMSD and their mixing state are equally important in estimating the aerosol direct radiative forcing, and suggested that the BCMSD should be fully considered in climate models. The method is a novel design and useful for understanding the relationship of BCMSD and their optical properties. The paper is interesting and well-organized. The conclusion is sound and may have profound impacts on the estimation of BC radiative forcing. I will recommend this manuscript for publication in ACP as long as the following comments are properly addressed.*

Reply: We thank the reviewer's comments.

Comment: *Specific comments: 1. Line 245 and fig. 2. It seems that the shift of particle peak diameter for BCPMSD is much more significant than PMSD. Is there any explanation? The correction procedure should be the same for both.*

Reply: We thank the reviewer's helpful comments. We checked the fig. 2 (now fig. 3 in the revised manuscript) and made some revisions in fig 2.

There are three methods to calculate the PMSD. The first one is the corrected PMSD that is transformed directly from the multiple-charging corrected PNSD with multiple-charging correction. If the aerosol PNSD is $\mathrm{n}(\mathrm{logD}_p) = \frac{dN}{dlogD_p}$, the corresponding PMSD after multiple-charging correction is:

$$\frac{\mathrm{dm}}{\mathrm{dlogD}_p} = n_V(\mathrm{logD}_p) \times \rho = V_p \times n(\mathrm{logD}_p) \times \rho = \frac{\pi}{6}\rho D_p^3 n(\mathrm{logD}_p) \qquad (1).$$

PMSD calculated in this method corresponds to the corrected PMSD in fig. R1.

The measured PNSD without multiple-charging correction can be calculated from the multiple charging corrected PNSD as:

$$(\frac{\mathrm{dn}}{\mathrm{dlogD}_p})_{raw} = \frac{\sum_{v=1}^{\infty} n(x_v)\emptyset(x_v,v)}{\emptyset(x_1,1)} \qquad (2),$$

Where $\mathrm{x}_v = \mathrm{logD}_{p,v}$ (noting that $\mathrm{x}_1 = \mathrm{logD}_p$); $\emptyset(x_v, v)$ is the probability of particles that are charged with v charges at the scale parameter of x_v; $\Omega(x, v)$ is the probability of particles that can pass through the DMA with v charges at the scale parameter x. The relationship between the x and v should meet the demand that their electrical mobility keep the same, ie

$$\mathrm{Z}_p(\mathrm{D}_{p,v}, \mathrm{v}) = \frac{veC(D_{p,v})}{3\pi\mu D_{p,v}} = \mathrm{Z}_p(\mathrm{D}_{p,1}, 1) \qquad (3),$$

where $C(D_p)$ is Cunningham slip correction:

$$\mathrm{C}(D_{p,v}) = 1 + \frac{2\tau}{D_{p,v}}(1.142 + 0.558e^{-\frac{0.999D_{p,v}}{2\tau}}) \qquad (4),$$

where τ is the gas mean free path.

The PMSD that corresponding to the measured PNSD can be calculated as

$$\left(\frac{\mathrm{dm}}{\mathrm{dlogD}_p}\right)_{raw} = \left(\frac{\mathrm{dV}}{\mathrm{dlogD}_p}\right)_{raw} \times \rho = \rho V_p \left(\frac{\mathrm{dn}}{\mathrm{dlogD}_p}\right)_{raw}$$

$$= \frac{\pi}{6}\rho D_p^3 (\frac{\mathrm{dn}}{\mathrm{dlogD}_p})_{raw} = \frac{\pi}{6}\rho D_p^3 \frac{\sum_{v=1}^{\infty} n(x_v)\emptyset(x_v,v)}{\emptyset(x_1,1)} \qquad (5).$$

The PMSD calculated using this method corresponds to the calculated PMSD in the fig. R1.

The third method for PMSD measured by DMA-CPC system is calculated as:

$$(\frac{\mathrm{dm}}{\mathrm{dlogD}_p})_{measure} = \frac{\sum_{v=1}^{\infty}\frac{\mathrm{dm}}{\mathrm{dlogD}_{p,v}}\emptyset(x_v,v)}{\emptyset(x_1,1)} = \frac{\sum_{v=1}^{\infty}\frac{\pi}{6}\rho D_{p,v}^3 n(x_v)\emptyset(x_v,v)}{\emptyset(x_1,1)} \qquad (6).$$

Equation 5 can be transformed into:

$$\left(\frac{\mathrm{dm}}{\mathrm{dlogD}_p}\right)_{raw} = \frac{\sum_{v=1}^{\infty}\frac{\pi}{6}\rho D_p^3 n(x_v)\emptyset(x_v,v)}{\emptyset(x_1,1)} = \frac{\sum_{v=1}^{\infty}\frac{\pi}{6}\rho D_{p,1}^3 n(x_v)\emptyset(x_v,v)}{\emptyset(x_1,1)} \qquad (7).$$

As $\mathrm{D}_{p,v}$ (*v=2,3,4* …) denotes the particle diameter with charged *v* that shares the same electrical diameter with Dp of single charged particle. Therefore, $\mathrm{D}_{p,v}$ (*v=2,3,4* …) is larger than $\mathrm{D}_{p,1}$, and the relationship of these PMSDs using different methods is

$$(\frac{\mathrm{dm}}{\mathrm{dlogD}_p})_{measure} > \left(\frac{\mathrm{dm}}{\mathrm{dlogD}_p}\right)_{raw} > \frac{\mathrm{dm}}{\mathrm{dlogD}_p} \qquad (8).$$

From fig. R1, the multiple-charging corrected PMSD is significantly different from the measured PMSD. Both the magnitude and peak location are changed. As shown in fig. R2 (fig. 3 in the manuscript), the variations of the BCMSD and PMSD show almost the same pattern before and after the multiple charging corrections.

We revised the text and figure 3 in the manuscript.

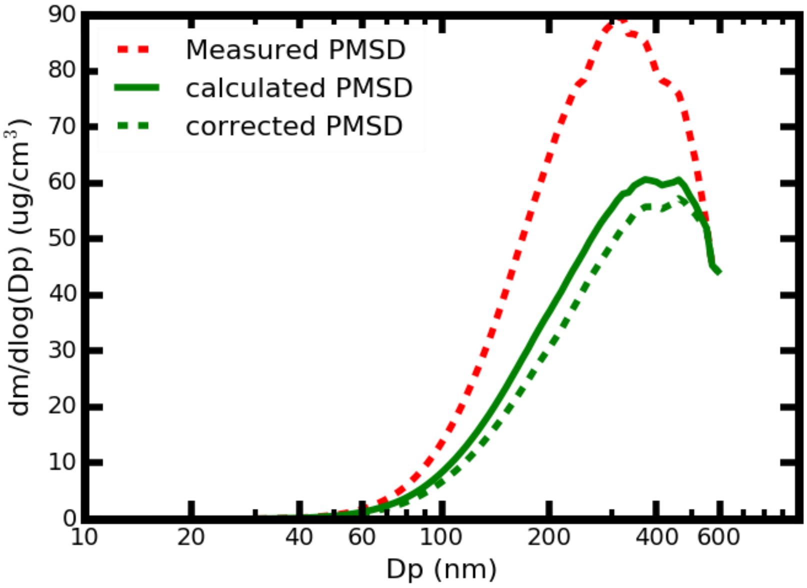

Fig. R1. Example of measured PMSD (in dotted read line), calculated PMSD from raw PNSD (in dotted green line) and corrected PMSD (in green line)

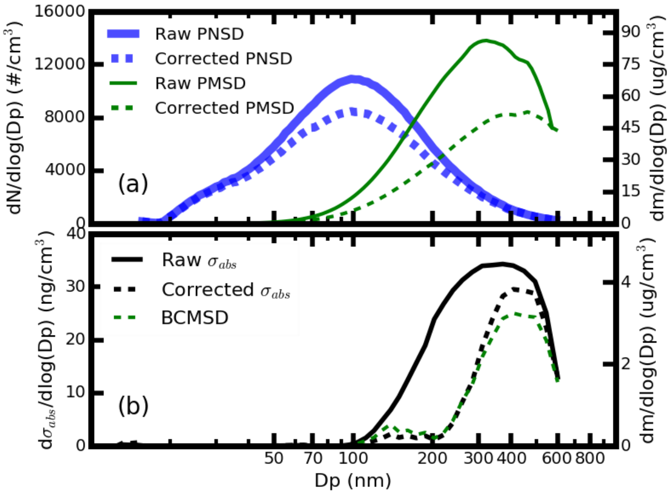

Figure R2. Case of multiple charging correction processing. (a) the multiple charging correction of the aerosol PNSD and aerosol PMSD, (b) the multiple charging correction of the size-resolved σ_{abs}. The solid line is the measured results without multiple charging corrections and the dotted line is the multiple charging corrections results.

Comment: *2. Line 306 and fig. 3. It looks strange that there is nearly no BC in the size range of 200nm-300nm. Any explanation? What does the PMSD look like? To me, it looks like the consequence of overestimation of multiple charging of BC. If the data is confirmed to be correct, proper explanation is necessary. Besides, the authors cited several SP2 measurement to support BC peak diameter range from 100nm to 200 nm. However, if I understand correctly, SP2 measures the diameter of BC core, while this study measures the size of entire particles. More references of studies with other methods may be needed.*

Reply: We thank the reviewer's comments. As described in reply of comment 1 and fig.R2, the multiple-charging corrections of the BCMSD is acceptable because the consequence of multiple charging of BCMSD is almost the same as that of the PMSD.

Our measurements show that the BCMSD has two modes with the coarser mode ranging between 430 nm and 580 nm in mobility diameter. Many field measurements have revealed that most of the BC mass locates in the aerodynamic diameter range of 320 nm and 560 nm using the MOUDI (Hu et al., 2012; Huang and Yu, 2008). When the aerodynamic diameter is transformed into mobility diameter with assumption a aerosol effective density of 1.3, the measured BC aerodynamic diameter range corresponds to mobility diameter range of 280 nm and 491 nm. Therefore, the measured size range for coarser mode of BCMSD agrees well with the previous measurement.

The measured aerosol in the field site is representative of the urban aerosol. The BC particles emitted by vehicles contribute significantly to the total aerosol BC mass. These BC particles are rarely coated or thinly coated, and the BC core diameter peaks around 120 nm (Zhang et al., 2017). Therefore, the BCMSD of the smaller mode measured in our study correspond to these uncoated of thinly coated particles.

We have revised the manuscript correspondingly.

Comment: *3. Line 48, I would add another BC microphysical property hygroscopicity in this sentence, which plays an important role in BC direct and indirect radiative forcing. (Zhang et al., 2008;Peng et al., 2017)*

Reply: We thank the reviewer’s comment. The manuscript has been revised correspondingly.

Comment: *4. Line 275: Please add full name of GSD.*

Reply: We thank the reviewer’s comment. We have revised the manuscript.

Comment: *5. Line 277, “wea” should be “was”*

Reply: Thanks for the comment. We have changed it.

Comment: *6. Line 279, should the BC density differ with different mixing state assumption? Externally mixed BC normally exhibits lower density. The authors can considered this as future improvement direction.*

Reply: We thank the reviewer’s helpful suggestions. The reviewer provided a good view of the possible direction that we should focus on.

Comment: *7. Line 329, “larger particles grew relative slower in diameter.” why? I would say larger particles grew slower in diameter in a log-normal scale. If this is what the authors meant, please verify.*

Reply: Thanks for the comment. For the aerosol particles smaller than 1 um, they grow by collision and coalescence. Coalescence is much more efficient than collision (Lamb and Verlinde, 2011). For coalescence, the mass growth ratio is in proportion to the square of the diameter (R^2). However, the growth of the volume is in proportion to the cubic of diameter (R^3). Therefore, the growth ratio of aerosol particles is in proportion to the R^{-1}, which means that the larger particles grow slower than these of smaller particles in diameter do. We agree with the reviewer’s idea that the larger particles appear to grow slower in a lognormal scale. We added some descriptions in the manuscript to denote it.

Comment: *8. Fig. 4 should be improved for better understanding by readership*

Reply: Thanks for the comment. We merged fig. 3 and part of fig. 4 into one figure.

Comment:*9. Fig. 6, is the figures made with the assumption of the same particle number concentration? If so, please verify.*

Reply: Thanks for the comment. The aerosol optical properties were calculated using the measured mean aerosol PNSD and different BCMSD. It was described in section 3.3. We added some descriptions in caption of fig. 6.

Comment:*10. Table 1. The mixing state here is assumed to be internally mixed, externally mixed, and core-shell mixed. But what is the mixing state assumption for the estimation with BCMSD?*

Reply: We thank the reviewer's comment. When estimating the radiative effects of BCMSD, we using the same mixing states of BC as that of Ma et al. (2012) in the North China Plain (NCP). Ma et al. (2012) found that the BC mixing states in NCP is partially core-shell mixed and partially externally mixed. The number ratio of the core-shell mixed BC particle and externally mixed particle is 0.51 Ma et al. (2012). We have added some descriptions in the manuscript.

Hu, M., Peng, J., Sun, K., Yue, D., Guo, S., Wiedensohler, A., Wu, Z. (2012) Estimation of size-resolved ambient particle density based on the measurement of aerosol number, mass, and chemical size distributions in the winter in Beijing. Environ Sci Technol 46, 9941-9947.

Huang, X.F., Yu, J.Z. (2008) Size distributions of elemental carbon in the atmosphere of a coastal urban area in South China: characteristics, evolution processes, and implications for the mixing state. Atmospheric Chemistry and Physics 8, 5843-5853.

Lamb, D., Verlinde, J. (2011) Physics and Chemistry of Clouds. Cambridge University Press, Cambridge.

Ma, N., Zhao, C.S., Müller, T., Cheng, Y.F., Liu, P.F., Deng, Z.Z., Xu, W.Y., Ran, L., Nekat, B., van Pinxteren, D., Gnauk, T., Müller, K., Herrmann, H., Yan, P., Zhou, X.J., Wiedensohler, A. (2012) A new method to determine the mixing state of light absorbing carbonaceous using the measured aerosol optical properties and number size distributions. Atmos. Chem. Phys. 12, 2381-2397.

Zhang, Y., Su, H., Kecorius, S., Wang, Z., Hu, M., Zhu, T., He, K., Wiedensohler, A., Zhang, Q., Cheng, Y. (2017) Mixing State of Refractory Black Carbon of the North China Plain
Regional Aerosol Combining a Single Particle Soot Photometer and
a Volatility Tandem Differential Mobility Analyzer. Atmospheric Chemistry and Physics Discussions, 1-27.

Role of black carbons mass size distribution in the direct aerosol radiative forcing

Gang Zhao[1], Jiangchuan Tao[2], Ye Kuang[2], Chuanyang Shen[1], Yingli Yu[1], Chunsheng Zhao[1*]

[1]Department of Atmospheric and Oceanic Sciences, School of Physics, Peking University, Beijing, China

[2]Institute for Environmental and Climate Research, Jinan University, Guangzhou 511443, China

Correspondence to: Chunsheng Zhao (zcs@pku.edu.cn)

Abstract

Large uncertainties exist when estimating radiative effects of ambient black carbon (BC) aerosol. Previous studies about the BC aerosol radiative forcing mainly focus on the BC aerosols' mass concentrations and mixing states, while the effects of BC mass size distribution (BCMSD) were not well considered. In this paper, we developed a method by measuring the BCMSD by using a differential mobility analyzer in tandem with an aethalometer. A comprehensive method of multiple charging corrections was proposed and implemented in measuring the BCMSD. Good agreement was obtained between the BC mass concentration integrated from this system and that measured in bulk phase, demonstrating the reliability of our proposed method. Characteristics of the BCMSD and corresponding radiative effects were studied based on field measurements conducted in the North China Plain by using our own designed measurement system. Results showed that the BCMSD had two modes and the mean peak diameters of the two modes were 150 nm and 503 nm respectively. The BCMSD of coarser mode varied significantly under different pollution conditions with peak diameter varying between 430 nm and 580 nm, which gave rise to significant variation in aerosol buck optical properties. The aerosol direct aerosol radiative forcing was estimated to vary by ~~22.5~~8.45% for different measured BCMSDs of coarser mode, which shared the same magnitude to the variation associated with assuming different aerosol mixing states (~~21.5~~10.5%). Our study reveals that the BCMSD matters as well as their mixing state in estimating the direct aerosol radiative forcing. Knowledge of the BCMSD should be fully considered in climate models.

1 Introduction

Atmospheric black carbon (BC) is the second strongest absorbing components in atmosphere (Bond et al., 2013) but the magnitudes of the warming effects are poorly quantified. When emitted to the surrounding, BC particles transform the morphology from fractal to spherical and then grow as fully compact particles with other components depositing on the BC aerosol (Peng et al., 2016). The variation in the shapes of BC aerosols, together with the variation in the mixing states, can lead to substantial change of aerosol optical properties (Liu et al., 2017;China et al., 2013;Wu et al., 2016a;Wu et al., 2018). BC aerosols also have significant influence on the climate by interacting with clouds (Koch and Del Genio, 2010;Roberts et al., 2008;Stevens and Feingold, 2009), ice and snow (Bond et al., 2013). Recent study shows that the solar absorption of BC can suppress the turbulence in the atmospheric boundary layer (Wilcox et al., 2016). It is found that BC emissions may be responsible for the incensement of droughts and floods in China and India (Menon et al., 2002). In addition, BC can pose a serve threat to human health through inhalation (Nichols et al., 2013;Janssen et al., 2011).

Comprehensive studies have been carried out to evaluate the climate effect of BC based on the measurement of BC mass concentrations (m_{BC}) (Koch et al., 2009;Ramanathan and Carmichael, 2008). The m_{BC} near the ground have been well characterized (Ramachandran and Rajesh, 2007;Ran et al., 2016b;Reddington et al., 2013;Song et al., 2013), and the BC vertical distributions are widely measured and evaluated as well (Ran et al., 2016a;Babu et al., 2011;Ferrero et al., 2011). Despite these measurements, more insights into the BC microphysical properties can help to estimate the influence of BC aerosols on visibility (Zhang et al., 2008), climate (Jacobson, 2001) and human health (Lippmann and Albert, 1969). These microphysical properties include BC morphology (Zhang et al., 2016), density (Zhang et al., 2016), complex refractive index (Bond et al., 2013), hygroscopicity (Zhang et al., 2008;Peng et al., 2017), mixing states (Moffet et al., 2016;Raatikainen et al., 2017), and particularly, the mass size distribution (BCMSD) (Cheng et al., 2012;Cheng and Yang, 2016;Gong et al., 2016). Knowledge of BCMSD is not only helpful to study the mixing state of BC aerosols (Raatikainen et al., 2017), but also essential to model the role of BC in evaluating regional and global climate accurately~~-~~. BC radiative effects is highly sensitive to the emitted BC particle size distribution (Matsui et al., 2018). The health impacts of BC are significantly related to BCMSD (Turner et al., 2015). Furthermore, the information of BCMSD can help to study the source, the evolution and the mixing state of ambient BC aerosols (Yu et al., 2010).~~However, few studies have focused on the characteristics of the BCMSD, and the BCMSD properties under different polluted conditions are not known yet.~~

Many methods have been proposed to measure the BCMSD. For instance, the BCMSD was measured by sampling the aerosol in the size range from about 50 nm to several micrometers onto quartz fiber filter substrates using a micro-orifice uniform deposit impactor (MOUDI) (Venkataraman and Friedlander, 1994;Guo, 2016). Cheng et al. (2014) developed a method to measure the BCMSD by employing two aethalometers in parallel, with one to measure total m_{BC} and the other to measure m_{BC} below specific particle sizes using a size cut-off inlet. The above two methods measure the BCMSD corresponding to the aerodynamic diameter. The Single Particle Soot Photometer (SP2) is developed and widely used because it provides sing particle information, hence the BCMSD and the mixing state of the atmospheric aerosols can be derived directly (Schwarz et al., 2006;Gao et al., 2007;Huang et al., 2012;Singh et al., 2016). –The BCMSD corresponding to the ambient aerosol mobility diameter can be measured by using a differential mobility analyzer (DMA) in tandem with SP2 (Raatikainen et al., 2017). However, the laser-induced incandescence method cannot provide reliable information about the particles beyond the range of 70 nm and 400 nm (Moteki and Kondo, 2010), which results in the lack of the knowledge of the BCMSD characteristics for these aerosols over 400 nm. The results from MOUDI find that a great amount of BC locates at the aerodynamic diameter range of ~~larger~~ between ~~than~~ 370 and 1000 nm (Hu et al., 2012;Huang and Yu, 2008). However, the measurements of MOUDI cannot give detailed information of the BCMSD evolution due to the low temporal and diameter resolution (Hu et al., 2012;Huang and Yu, 2008). The characteristics of the BCMSD larger than 370 nm is not well studied due to the limitation of the instrument.

Recently, Ning et al. (2013) and Stabile et al. (2012) proposed a new method to measure the BCMSD by using differential mobility analyzer (DMA) in tandem with Aethalometer (AE). This method has the potential of measuring the BCMSD from 20 nm to 584 nm with high time resolution. We develop and validate the BCMSD measurement system based on the works of Ning et al. (2013). The developed measurement system was employed in a field campaign in the North China Plain. The characteristics of the measured BCMSD were studied based on the field measurement. Furthermore, the effects of BCMSD variations on the aerosol optical properties and corresponding direct aerosol radiative properties were evaluated. The aerosol optical properties were calculated by using the Mie scattering theory. The direct aerosol radiative forcing (DARF) were estimated by using the Santa Barbara DISORT (discrete ordinates radiative transfer) Atmospheric Radiative Transfer (SBDART) model.

The structure of this paper are organized as follows. Section 2 gives the information about the instrument setup and field measurement. Section 3 gives the detailed method used in this study, which contains: 1, conducting multiple charging corrections when deriving the aerosol BCMSD and 2, evaluating the aerosol optical and radiative properties for different BCMSD. Results and discussions are shown in section 4. The conclusion is drawn in the last part.

2 Instrument Setup

The measurement system setup was based on the works of Stabile et al. (2012) and Ning et al. (2013) as schematically shown in Fig.1. The ambient sample aerosol particles were firstly dried to below relative humidity of 30% through a Nafion drying tube before passing through to the DMA (Model 3081, TSI, USA). The DMA scanned aerosol particles with diameter ranges from 12.3 to 697 nm over a period of 285 seconds and started another scanning after a pause of 15 seconds, so one complete cycle took 5 minutes. The sheath and sample flow rates of the DMA were 3 lpm and 0.5 lpm, respectively. The quasi-monodisperse aerosols that passed through the DMA were further divided into two flows: with one lead to an aethalometer (AE51, Model 51, MicroAeth, USA) with a flow rate of 0.2 lpm to measure the ~~–~~absorption coefficient (σ_{abs}) at 1 second time resolution; and the other one with flow rate of 0.3 lpm flow directed to a CPC (Model 3772, TSI, USA), which counted particle number concentrations at 0.1 second resolution. Clean air with a flow rate of 0.7 lpm was used to compensate for the CPC inlet flow, which had default flow rate of 1 lpm. Overall, the combination system of DMA, CPC and AE51 could provide one PNSD and ~~BCMSD~~ size-resolved σ_{abs} scan every 5 minutes. If the mass absorption coefficient (MAC) at a given diameter is known, the BCMSD can be derived correspondingly.

A~~t the same time, another~~n aethalometer (AE33, Model 33, Magee, USA) was used to measure the σ_{abs} or m_{BC} with a time resolution of 1 minute. The mass concentration of particles with diameter smaller than 2.5 μm (PM2.5) was concurrently measured with time resolution of 1 minute during the filed observations by the Tapered Element Oscillating Microbalance (TEOM) Dichotomous Ambient Particulate Monitor (1405-DF), which was an indicator of the pollution conditions.

From 21 March to 9 April in 2017, an intensive field measurement was conducted to characterize of the ambient dry aerosol BCMSD corresponding to aerosol mobility diameter at the AERONET BEIJING_PKU station (N39°59′, E116°18′). This station was located on one roof of Peking University campus in the north west of Beijing, China. There were two main streets, Chengfu

Road to the south and Zhongguancun Street to the west that surrounding the station. The aerosol sampled at this station were mainly composed of urban roadside aerosols (Zhao et al., 2018).

3 Methodologies

3.1 Retrieving the BCMSD

~~Four~~ Five steps were involved to calculate the BCMSD using the raw data from the measurement system: 1), correcting the 'loading effect' and 'multiple scattering effect' of σ_{abs}~~m_{BC}~~ measured by AE51; 2), matching the instrument time between the AE51 and CPC; 3), matching the measured σ_{abs}~~m_{BC}~~ and diameter to get the raw ~~BCMSD~~size-resolve σ_{abs} that is not involved in multiple charging corrections; 4), conducting the multiple charging corrections of the measured raw ~~BCMSD~~size-resolved σ_{abs}; 5), transforming the size-resolved σ_{abs} intto BCMSD.

3.1.1 Obtaining the raw ~~BCMSD~~size-resolved σ_{abs}

The aethalometer (AE51 and AE33) is a well-developed and widely used instrument to measure the σ_{abs}~~m_{BC}~~ (Drinovec et al., 2015;Hansen et al., 1984). When absorbing aerosols accumulates on the sample filter of the aethalometer continuously, the σ_{abs}~~m_{BC}~~ can be determined by concurrently measuring the light intensities *I* after the fiber filter and the light intensities I_0 transmitted through reference spot which is free of aerosol loading. The light attenuation (ATN) is defined as:

$$\mathrm{ATN} = 100 \cdot \ln(\frac{I_0}{I}). \tag{1}$$

The total σ_{abs} ~~mass of BC~~ of the loaded particle ~~–~~ on the filter is given by:

$$\sigma_{abs,tot}\cancel{m_{BC,load}} = \frac{\mathrm{A \cdot ATN}}{100\cancel{\cdot\sigma_{BC}}}, \tag{2}$$

where A is the sample spot area on the filter ~~and σ_{BC} is the mass attenuation cross-section of BC~~. The instantaneous σ_{abs} can be calculated through ~~The equivalent $\mathrm{m_{BC}}$ can be calculated through~~ the increment of $\sigma_{abs,tot}$~~$m_{BC,all}$~~:

$$\sigma_{abs}\cancel{m_{BC}} = \frac{\sigma_{abs,tot}\cancel{m_{BC,load}}}{\Delta t} = \frac{A \cdot \Delta ATN}{100\cancel{\cdot\sigma_{BC}}\cdot F \cdot \Delta t}, \tag{3}$$

where F is the flow rate and ΔATN is the ATN variation during the time period of Δt. The $\sigma_{abs,tot}$ can be transformed to m_{BC} when the mass attenuation cross-section (MAC) of BC is known. Traditionally, a constant MAC at 7.7 g/m^2 was used to deduce the m_{BC} (Drinovec et al., 2015).

Corrections of the measured σ_{abs} are necessary because the systematic bias exists due to the prevailingly known 'loading effect' and multiple scattering effect (Drinovec et al., 2015;Virkkula et al., 2015;Virkkula et al., 2007). The AE33 can directly provide the corrected σ_{abs}~~m_{BC}~~ values through measuring two light intensities of two spots with different BC load efficiencies (Drinovec et al., 2015). For AE51, The correcting method in Virkkula et al. (2007) was adopted:

$\sigma_{abs,\ corrected}$~~$m_{BC,corrected}$~~ $= (1 + \mathrm{k} \times ATN)\sigma_{abs,uncorrected}$~~$m_{BC,uncorrected}$~~, (4)

where k is the correction factor and a constant value of 0.004 is employed in this study to correct the σ_{abs}~~m_{BC}~~ from AE51. In the first part of the supplementary material, we showed that the loading effects corrections of σ_{abs}~~m_{BC}~~ from AE51 were essential and the value of σ_{abs}~~m_{BC}~~ from AE33 could be used as a reference for the measured BCMSD. As for the multiple scattering corrections, Zhang et al. (2018) compared the measured σ_{abs} measured by AE33 and by Multi-Angle Absorption Photometer (MAAP) at Tsinghua University, which is about 2 km away from our measurement site. They recommended a compensation factor of 2.6 to be used and we adopted the same factor in our study.

Time correction was needed because time gaps between voltages implied on the DMA (particle size) and sample particles measured by different instruments were not the same. The time correction procedures were conducted every day during the field measurement to ensure that the time deviations of the CPC and the AE51 were constrained within 2 seconds.

Fig. S3 gave the time series diagram of scanned aerosol diameters by DMA, measured σ_{abs}~~m_{BC}~~ from AE51, and the aerosol number concentrations counted by CPC. The aerosol PNSD (or ~~BCMSD~~size-resolved σ_{abs}) could be calculated by matching the DMA diameter and the measured aerosol number concentrations (or measured σ_{abs}~~m_{BC})~~ by simply using the single particle charge ratio for each electrical mobility diameter. These measured PNSD and ~~BCMSD~~ size-resolved σ_{abs} did not consider the effect of multiple-charging corrections and are labeled as raw aerosol PNSD and raw aerosol size-resolved σ_{abs}. ~~BCMSD.~~

3.1.2 Multiple charging corrections of raw size-resolved σ_{abs}~~BCMSD~~

In the work of Ning et al. (2013) study, lots of efforts were made to evaluate the performance of the instrument. They considered the diffusion corrections and particle charging corrections. However, the particle charging corrections were limited to single particle charge ratio as they mentioned that they simplified the particle charge correction by applying the peak electrical mobility for the calculation of representative particle size for each mobility bin and single particle charge ratio for each primary mobility. They ignored the fact that the aerosol samples selected by the DMA were quasi-monodisperse with different charges and different diameters.

We proposed a new algorithm for the multi-charge corrections of the ~~BCMSD~~size-resolved σ_{abs}. Multi-charge corrections to the measured size distribution were prevailing when the DMA was used to scan the aerosol sizes. When the DMA and CPC are used together to measure the aerosol particle number size distribution (PNSD), the multi-charging corrected aerosol PNSD can be significantly different from the raw measured one (Bau et al., 2014;He and Dhaniyala, 2013;He et al., 2015). As shown in the results part of this study, the multi-charge corrections of the ~~BCMSD~~ size-resolved σ_{abs} could cause differences in both the magnitude and shape of the ~~BCMSD~~size-resolved σ_{abs}. Therefore, it is necessary to perform multi-charge corrections on the size-resolved σ_{abs}~~BCMSD~~. This study developed a new algorithm to correct the size-resolved σ_{abs}~~m_{BC}~~ from measured value~~from measured m_{BC}~~ based on the work of Hagen and Alofs (2007) and Deng et al. (2011).

When the DMA is charged with a negative voltage, those aerosols with a small range of electrical mobility (Z_P) can pass through the DMA:

$$Z_P = \frac{q_{sh}}{2\pi VL}\ln\left(\frac{r_1}{r_2}\right), \quad (5)$$

where q_{sh} is the sheath air flow rate; V is the average voltage on the inner center rod; r_1 and r_2 are the outer and inner radius of annular space respectively. The Z_P is related with D_p by elementary charge (e), number of elementary charges on the particle (n), and gas viscosity poise (μ) with:

$$Z_p = \frac{neC(D_p)}{3\pi\mu D_p}, \quad (6)$$

where $C(D_p)$ is Cunningham slip correction:

$$\mathrm{C} = 1 + \frac{2\tau}{D_p}\left(1.142 + 0.558e^{-\frac{0.999D_p}{2\tau}}\right), \quad (7)$$

where τ is the gas mean free path. From equation 7, aerosol particles can have the same Z_P despite that they have different n and D_p. At the same time, there exists a relatively larger portion of multiple charged particles for those particles with diameters between 100 nm and 400 nm when the ambient aerosols pass through the X-ray (Tigges et al., 2015;Wiedensohler and Fissan, 1988). Through the above discussion, the selected aerosols by DMA at a given electrical mobility can have different charges which will correspond to different diameters.

When the scan diameter is set as Dp_i for the singly charged particles and the respective voltage of DMA is V_i (i =1, 2, …, I), aerosol particles with electro-mobility of $Z_{p,i}$ (i=1, 2, …, I) can pass through the DMA and the observed σ_{abs}~~m_{BC}~~ by AE51 can be expressed as:

$$R_i = \int_0^{\infty} G(i,x)A(x)n(x)dx, \tag{8}$$

where x is the scale parameter, with the definition of $x = \log(Dp_i)$, A(x) is the average~~ BC~~ σ_{abs}~~mass concentration~~ of single particle~~s~~ for scale parameter x, and $n(x) = dN/d\log Dp$ is aerosol PNSD that is the multiple charging corrected results from the measured aerosol PNSD. We define the kernel function G (i, x), which is crucial to the algorithm, as:

$$G(i,x) = \sum_{v=1}^{\infty} \emptyset(x,v)\Omega(x,v,i), \tag{9}$$

where $\emptyset(x,v)$ is the probability of particles that are charged with v charges at the scale parameter of x (Wiedensohler, 1988). $\Omega(x,v,i)$ is the probability of particles that can pass through the DMA with v charges at the scale parameter x (Knutson and Whitby, 1975). In this study, the maximum value of v is 10.

The multiple charging corrections can be expressed as computing the $A(x_i^*)$, in which x_i^* is the predetermined scale parameter from the DMA. To get the numerical integration results of equation 9, the diameter interval that is 1/50 of the measured diameter is used. Thus, equation 9 can be written as

$$R_i = \int_0^{\infty} G(i,x)A(x)n(x)dx = \Delta x_i \sum_{j=1}^{50} \beta_j G(i,x_{i,j})A(x_{i,j})n(x_{i,j}), \tag{10}$$

where $\beta = \{\begin{matrix} 0.5, & j = 1, J \\ 1, & otherwith \end{matrix}$; $x_{i,j}$ is the jth (j=1 ,2 ,…, 50) parameter that locates at the parameter x_i and x_{i+1} and $A(x_{i,j})$ (i=1, 2, …, I; j=1, 2, …, 50), the BC mass ratio at scale parameter $x_{i,j}$, is expressed as the linear interpolation of the values at the measured diameters.

$$A(x_{i,j}) = A(x_i) + P_i(x_{i,j} - x_i), \tag{11}$$

where P_i is the slope of the linear interpolation result of

$$A(x_k^*) = C + P_i \cdot x_k^*. \tag{12}$$

x_k^* refers to these five diameters that are nearest to the predetermined scale parameter x_i. C is the intercept of the linear interpolation result.

With $H_{i,j} = \beta_j \Delta x_i G(i,x_{i,j})n(x_{i,j})$, equation 11 can be written as

$$R_i = \sum_{j=1}^{J} H_{ij}\left[A(x_i) + P_i(x_{i,j} - x_i)\right] = \sum_{j=1}^{J} H_{ij}A(x_i) + \sum_{j=1}^{J} H_{ij}\, P_i x_{i,j} - \sum_{j=1}^{J} H_{ij}\, P_i x_i$$

$$= \sum_{k=1}^{I}(\sum_{j=1}^{J} H_{ij}\, \delta(i-k))A(x_k^*)) + \sum_{k=1}^{I}\left(\sum_{j=1}^{J} H_{ij}\, x_{i,j}\delta(i-k)\right) P_k - \sum_{k=1}^{I} \delta(i-\ k)))P_k x_k^*$$

$$=\sum_{k=1}^{I} Q_{ik} A(x_k^*) + \sum_{k=1}^{I} T_{ik} P_k - \sum_{k=1}^{I} Q_{ik} P_k x_k^*, \qquad (13)$$

where $\delta(x)=\begin{cases}0, x\neq 0\\ 1, x=0\end{cases}$,

$$Q_{ik} = \sum_{j=1}^{J} H_{ij}\,\delta(i-k), \qquad (14)$$

and $$T_{ik} = \sum_{j=1}^{J} H_{ij}\, x_{i,j}\, \delta(i-k). \qquad (15)$$

By letting the

$$S_i = R_i - \sum_{k=1}^{I} T_{ik} P_k + \sum_{k=1}^{I} Q_{ik} P_k x_k^*. \qquad (16)$$

This equation is then expressed as

$$S_i = \sum_{k=1}^{I} Q_{ik} A(x_k^*), \qquad (17)$$

or

$$S = QA, \qquad (18)$$

where S and A are $I \times 1$ vectors and Q is an $I \times I$ matrix. This matrix can be solved by using the non-negative least square method.

Finally, the A(x) can be determined and the corresponding size-resolved σ_{abs}~~BCMSD~~ that is multiple charging corrected can be calculated.

3.1.3 Transform the size-resolved σ_{abs} into BCMSD

MAC of different size range is necessary when transform the size-resolved σ_{abs} into BCMSD. The MAC at different size should be different. When the size-resolved σ_{abs} is converted into BCMSD with a constant MAC, the derived BCMSD would be biased.

The size-resolved MAC was calculated using the Mie scattering model (Bohren and Huffman, 2007). Based on the Mie scattering theory, MAC values vary for different aerosol core diameter and different total diameter. Results from SP2 measurement show that the size distribution of the BC core diameter peaked at around 120 nm in Beijing (Zhang et al., 2017). For each aerosol diameter, the MAC value with core diameter of 120 nm was used to transform the BCASD into the BCMSD. MAC values with core diameter at 120±15 nm were calculated and shown in Fig. 2. From Fig. 2, the MAC varied significantly between 3.6 and 9.2 m^2/g. The constant MAC values 7.7 m^2/g corresponded to the aerosol diameter of 269 nm. The calculated mean MAC values in Fig. 2 under different diameter were used in this study.

3.1.~~3~~4 Validation of the multiple charging corrections

An example of the multiple charging corrections of the size-resolved σ_{abs} was shown in Fig. ~~2~~3.

The corrections of aerosol PNSD were based on the work of Hagen and Alofs (2007). As shown in Fig. 2(a), the corrected aerosol PNSD was significantly different from the original uncorrected one. There were about half of the measured particles have multiple elementary charge in the size range between 100 and 200 nm. The raw uncorrected aerosol PNSD had a peak value of 10920 cm^{-3} at 98 nm while the corrected aerosol PNSD reached its peak value of 8450 cm^{-3} at 98 nm. The peak positions of the raw aerosol particle mass size distribution (PMSD, dm/dlogDp) peaked at ~~371nm~~ 322 nm with a peak value of ~~56~~ 86.3 μg/m^3 and the corrected aerosol PMSD had a peak value of 53 μg/m^3 at ~~445~~ 461 nm. The peak position of the aerosol PMSD shifted a lot before and after the multiple charging corrections. The similar case for the ~~BCMSD~~ size-resolved σ_{abs} was shown in Fig. 2(b). The shape of size-resolved σ_{abs}~~BCMSD~~ had changed substantially due to the multiple charging corrections. The measured raw BCMSD had a peak diameter near 320~~00~~ nm and the magnitude of size-resolved σ_{abs}~~BCMSD~~ plateau reached ~~6000 ng/m^3 at 283nm~~34.3 Mm^{-1}, which was in accordance with the results of Ning et al. (2013), where the multiple charging corrections were not involved. However, the corrected size-resolved σ_{abs}~~BCMSD~~ peaks near ~~400nm~~410 nm, with a peak value of about ~~5500 ng/m3 at 407nm~~29.5 Mm^{-1}. According to the result, a small amount of σ_{abs} ~~BC~~ remained in particles with diameter between 100nm and 200nm. The measured size-resolved σ_{abs}~~BCMSD~~ changed a lot when multiple charging corrections were implemented, which highlighted the necessity of implementation of appropriate multiple charging corrections

The σ_{abs}~~m_{BC}~~ integrated from measured size-resolved σ_{abs}~~BCPMSD~~ changed after multiple charging corrections. Fig. S4 showed the comparison results of the σ_{abs}~~m_{BC}~~ measured by AE33 and the~~–~~ σ_{abs}~~m_{BC}~~ integrated from AE51 measurements. The σ_{abs}~~m_{BC}~~ integrated from uncorrected and corrected size-resolved σ_{abs}~~BCMSD~~ versus σ_{abs}~~m_{BC}~~ measured by AE33 were shown in Fig.S4(a) and Fig.S4(b), respectively. Before multiple charging corrections, the σ_{abs}~~m_{BC}~~ from uncorrected size-resolved σ_{abs}~~BCPMSD~~ increased linearly with the σ_{abs}~~m_{BC}~~ from AE33, with R^2 equaling 0.87, but it was 2.37 times that of AE33 in average. As a comparison, overall magnitude of σ_{abs}~~m_{BC}~~ integrated from corrected size-resolved σ_{abs}~~BCPMSD~~ agreed better with that from AE33 with a slope of 1.2. With the discussion above, multiple charging corrections were essential for size-resolved σ_{abs} and BCMSD measurements.

3.2 Fitting the BCMSD by using two log-normal models

Based on the measurement results, the BCMSD had two modes for most of the conditions. The

BCMSD are assumed to be of two log-normal distributions as:

$$m_{fit,Dp} = \sum_{i=1,2} \frac{m_i}{\sqrt{2\pi}\log(GSD_i)} \cdot \exp\left(-\frac{[\log(D_p)-\log(D_{m,i})]^2}{2log^2(GSD_{,i})}\right), \qquad (19)$$

Where D_p is the diameter of the aerosols; m_i is the mass of mode i (i=1,2); GSD_i is the geometric standard deviation at mode i (i=1,2), and $D_{m,i}$ is the geometric mean diameter of the mode i (i=1,2). The GSD_i and $D_{m,i}$ can be determined by using the least square method with the objective function as :

$$\mathrm{J} = \sum_{i=1,n}\left(m_{Dp_i} - m_{fit,Dp_i}(D_{m1}, GSD_1, D_{m2}, GSD_2)\right)^2, \qquad (20)$$

Where m_{Dp_i} is the measured mass distribution at Dp_i, while m_{fit,Dp_i} is the fit mass distribution at Dp_i.

3.3 Estimating aerosol optical properties with different BCMSD

The Mie scattering model was used to study the influence of the BCMSD variation on the aerosol optical properties. When running the Mie model, aerosol PNSD and BC were necessary. ~~The aerosol PNSD and m_{BC} used here is the mean result of aerosol PNSD and m_{BC} over the whole field measurement respectively. The amount of BC particle adopted in this study is the mean value of the m_{BC} measured by AE33.~~ In this study, The BCMSD was assumed to be log-normal distributed. D_m of the BCMSD was set to vary from 100 nm to 600 nm. Geometric standard deviation (GSD) of the BCMSD was set to be in the range between 1.3 and 1.8. BC was treated as partially externally mixed and the remaining aerosols was treated as core-shell mixed. The ratio of externally mixed m_{BC} to core-shell m_{BC} was~~ea~~ determined by the method introduced in Ma et al. (2012) and a mean ratio of 0.51 was used. The density and refractive index of BC were set as 1.5 g/cm3 and 1.8+0.54i (Kuang et al., 2015), respectively. The complex refractive index of non-absorbing aerosols was 1.53+10-7i (Wex et al., 2002) at the wavelength of 525 nm. More details of calculating the aerosol optical properties by using the aerosol PNSD and BCMSD, can refer to Kuang et al. (2016).

The aerosol PNSD and m_{BC} used here is the mean result of aerosol PNSD and m_{BC} over the whole field measurement respectively. The amount of BC particle adopted in this study is the mean value of the m_{BC} measured by AE33. For each BCMSD, extinction coefficient (σ_{ext}), the scattering coefficient (σ_{sca}), the single scattering albedo (SSA), and the asymmetry factor (g) could be obtained from the output of Mie scattering model.

3.4 Evaluating the DARF with different BCMSD

In this study, the SBDART model (Ricchiazzi et al., 1998) was employed to estimate the DARF. In our study, the instantaneous DARF for cloud free conditions at the top of atmosphere was calculated for irradiance wavelength range from 0.25 to 4 μm. Input of the model required the profiles of aerosol σ_{ext}, SSA, g. These ~~values~~ profiles were calculated ~~by~~ from the ~~parameterized aerosol PNSD, BCMSD profiles~~ parameterization of the aerosol vertical distributions. Details of calculating the σ_{ext}, SSA and g profiles can refer to part 4 in the supplementary material. ~~The corresponding DARF for different BCMSD could be estimated.~~ In brief, the aerosol σ_{ext}, SSA and g profiles were calculated based on the given aerosol PNSD and BCMSD. The DARF can be estimated using the above aerosol optical profiles.

The aerosol optical properties and the corresponding aerosol optical profiles vary with different BCMSD. Then the DARF should be different for different BCMSD. By estimating the DARF using different aerosol BCMSD, the influence of BCMSD on the aerosol radiative properties can be studied. ~~More details of estimating the DARF could refer to part 4 and 5 in the supplementary material.~~ The corresponding DARF for different BCMSD could be estimated. ~~The DARF was estimated for the measured mean aerosol PNSD and m_{BC} under different BCMSD conditions to study the effects of BCMSD variations on the aerosol DARF.~~

4 Results and Discussions

4.1 Measurement results of the BCMSD

The time series of measured PM2.5, aerosol PNSD and BCMSD were shown in Fig. 3. During the observation period, the PM2.5 varied from 0.06 to 220 μg/m^3, with a mean value of 71.5±52.56 μg/m^3. Three periods of heavy PM2.5 loading were observed: (1) PM2.5 increased from around 100 μg/m^3 to 200 μg/m^3 and decreased slowly to 1 μg/m^3 in the period 21-26, March; (2) the PM2.5 accumulated slowly from 28 to 30, March and dissipated quickly from 30, March to 1, April; (3) the rapid accumulation and dissipation of PM2.5 happened during 2 to 5, April. During the last five days, PM2.5 fluctuated between 20 and 120 μg/m^3. For each pollution condition, both the aerosol total number concentrations and the aerosol median diameter increased. The aerosol median diameter varied between 31 nm and 169 nm with a mean value of 78±31 nm.

~~As for the BCMSD, a distribution with two modes could be detected.~~ Our measurements shew that the BCMSD had two modes with the coarser mode ranging between 430 nm and 580 nm in mobility diameter. Many field measurements had revealed that most of the BC mass locates in the aerodynamic diameter range of 320 nm and 560 nm using the MOUDI (Hu et al., 2012;Huang and Yu, 2008). When the aerodynamic diameter was transformed into mobility diameter with assumption a aerosol effective density of 1.3, the measured BC aerodynamic diameter range corresponded to mobility diameter range of 280 nm and 491 nm. Therefore, the measured size range for coarser mode of BCMSD agreed well with the previous measurement.

The measured aerosol in the field site was representative of the urban aerosol. The BC particles emitted by vehicles contributed significantly to the total aerosol BC mass. These BC particles were rarely coated or thinly coated, and the BC core diameter peaked around 120 nm (Zhang et al., 2017). Therefore, the BCMSD of the smaller mode measured in our study corresponded to these uncoated of thinly coated particles. ~~The presence of the first mode in the size range between 100 and 200 nm provided a verification of previous field measurements that the BC concentrated in the particle diameter range from 100 to 200 nm. (Huang et al., 2012;Ohata et al., 2011;Wu et al., 2016b). The peak diameter of second mode ranged from 300 nm to 600 nm, which agrees well with the measured BCMSD by MOUDI (KlausWilleke and Baron, 1996;Yu and Yu, 2009;Huang and Yu, 2008). The main BC mass loading was in the coarser mode for the sampled particles when comparing the BC mass concentrations at two modes.~~

The total m_{BC} measured by AE33 ranged from 0.1 to 14 μg/m^3 with an average of 5.04 ± 2.64 μg/m^3. Good consistence was achieved between m_{BC} measured by AE33 and m_{BC} calculated from measured BCMSD as shown in Fig. 3~~4~~(~~c~~d).

4.2 Evolution of the BCMSD under different polluted conditions

Log-normal distribution was used to fit each mode of the BCMSD by using the least square method as introduced in section 3.2. For each mode, the geometric mean diameter (D_m) and the geometric standard deviation (GSD) of the BCMSD were studied.

During the measurement period, both D_m and GSD of the two modes had changed significantly as shown in Fig ~~4~~S7. The D_m of first and second mode varied from ~~128~~ 139 to ~~162~~ 161 nm and from ~~430~~ 420 to ~~580~~ 597 nm, respectively. The corresponding mean D_m was ~~150~~ 151 and ~~503~~ 520 nm. The D_m of the two modes was found to be positive correlated in Fig. ~~4a~~S7(a). When the pollution was released from the beginning to 27, March, the D_m decreased from ~~590to~~ 597 to 420 nm and from ~~155~~ 160 to ~~130~~ 140 nm for the coarser mode and the smaller mode respectively. The BC containing aerosols tended to be aged and grew larger when the air surrounding get polluted.

GSD for the coarser mode and the smaller mode showed very different properties as shown in Fig. ~~4b~~S7(b). For the second mode, GSD varied from around 1.49 to 1.68 with a mean value of 1.57. The GSD get decreased with the pollution condition, which indicated that BC containing aerosols tend to accumulate to a small range of diameters during the aging processing. This phenomenon was consistent with the fact that larger particles grew relative slower in diameter because the growth ratio of small aerosol particle is proportion to the negative power of it's diameter. For the first mode, GSD ranged from 1.~~5~~ 41 to around 1.~~85~~ 86 with a mean value of 1.~~62~~63. However, GSD of the smaller mode tend to be larger when the surrounding air get cleaner, which might be related to the complex sources of the BC emission. A small amount of fresh emitted BC particles can have substantial influence on the mass size distribution of the smaller mode because the BC concentrations of the smaller mode were small, especially under clean conditions. In general, the GSD of coarser mode was a good indicator of the BC aging process and that of the smaller mode could partially reflect the complex sources of the BC fine particles.

The relationship between the D_m and the GSD for coarser mode was further analyzed by analyzing the distribution of the D_m and GSD. The GSD and D_m had opposite trends as shown in Fig 5. With the increment of the D_m from 420 to 540 nm, the mean value of GSD decreased from around 1.608~~5~~ to 1.~~548~~ 528 while the m_{BC} increased with the D_m. The statistical relationship between D_m and GSD offered a reasonable representation of the BCMSD under different polluted conditions. In the following work, mean values of the GSD at different D_m were used to for further discussion. The m_{BC} and GSD is positively correlated. The m_{BC} increased from 2.4 to 8.3 µg/m^3 when the D_m increased from 420 to 540 nm.

Note that the GSD get slightly increased with the increment of D_m when D_m was larger than 520 nm. This might be caused by the limit diameter range of BCMSD measuring system which was from 20 to 680 nm. The multiple charge corrections applied to the BCMSD could influence the BCMSD when D_m of the BCMSD was near the end of the scanned diameter and may lead to significant uncertainties to the BCMSD. The measurement results indicated that cases of measured D_m of BCMSD larger than 520 nm were few, demonstrating that this multiple correction effect influenced little on shape of measured BCMSD in most cases.

4.3 Influence of BCMSD variation on the aerosol optical properties

The aerosol optical parameters using the measured mean aerosol PNSD and mean m_{BC} corresponding to different GSD and D_m values were shown in Fig. 6. In Fig. 6(a), the aerosol g varied from 0.~~617 ~~603 to 0.~~649 ~~627 (variation of ~~5.8~~4%). Recent work by Zhao et al, 2017 showed that the aerosol g value in the NCP may vary at a range of 10% due to the change of aerosol PNSD. Aerosol g was more sensitive to D_m when the geometric mean diameter of the BCMSD was lower than 400 nm. However, when the D_m was larger than 400 nm, the g become sensitive to both the D_m and the GSD of BCMSD. Overall, the g varied a little bit (0.~~617 ~~02 to 0.~~624~~609) under the representative conditions during the measurement period. For the aerosol SSA, it was sensitive to the D_m over the whole range as shown in Fig. 6(b). SSA varied between 0.~~86 ~~90 and 0.~~88 ~~94 under the representative measurement conditions. The σ_{sca} had large changes from ~~264 ~~325.6 Mm^{-1} to ~~313~~ 364.4 Mm^{-1}. The σ_{sca} was quite sensitive to variations in BCMSD when the D_m was ~~lower ~~larger than ~~400 ~~450 nm as shown in Fig.6c~~, which varied substantially from 264 Mm^{-1} to 313 Mm^{-1}~~. In addition, variations in σ_{sca} relied more on the variations in D_m when D_m was ~~larger ~~lower than 400 nm. Within the measurement conditions of BCMSD, the σ_{sca} varied from ~~265 ~~328 Mm^{-1} to ~~280 ~~345 Mm^{-1}. The measured GSD under different D_m went along with the gradient direction of the σ_{sca}, which mean that the evolution of BCMSD in the atmosphere influenced substantially on σ_{sca}. As for the σ_{abs}, it changed from 2~~1.94~~4.06 Mm^{-1} to ~~44.12~~37.27 Mm^{-1} and the corresponding mass absorption cross section (MAC) was estimated to be in the range of ~~4.75~~5.44 to ~~9.56~~8.08 m^2/g, suggesting that MAC of the BC aerosols should be carefully studied under different BCMSD conditions.

4.4 Influence of BCMSD on the direct aerosol radiative forcing

The estimated DARF values for different GSD and D_m conditions were estimated. When estimating the DARF, the measured mean aerosol PNSD and mean BC mass concentration were used~~-~~. The results of estimated DARF were shown in Fig. 7(a). DARF at the surface varied from -~~4.90 ~~-4.3 w/m^2 to ~~-2.02~~-3.59 w/m^2 for different BCMSD. Within the measured BCMSD range, the DARF varied from ~~-2.04w~~-3.97w/m^2 to -~~2.5~~3.67w/m^2, which corresponding to ~~22.5~~8.45% of variation. The heating rate within the mixed layer was a powerful indicator of the BC particles' absorbing effects, which may help evaluate the development of the boundary layer. The calculated mean heating rate within the mixed layer changed from ~~3.25~~2.16 K/day to ~~3.89~~2.65 K/day for different D_m and GSD, as shown in Fig. 7(b). The heating rate with the measured BCMSD range could change from ~~3.56~~2.24 to ~~3.75~~2.50 with a variation of ~~5.23~~11.6%.

Mixing states of BC play significant roles in calculations of aerosol optical properties and estimations of DARF (Jacobson, 2001). As a comparison, we estimated the DARF under different conditions of BC mixing state: (1) internally mixed, (2) externally mixed and (3) core-shell mixed. Table 1 gave the estimated DARF and mean heating rate within the mixed layer under different mixing state conditions. Results showed that the DARF under different BC mixing states conditions may change by ~~21.5~~10.50%, which shared the same magnitude with ~~22.5~~8.45% variation of DARF caused by BCMSD variations. In addition, the heating rate was estimated to vary by ~~6.05~~9.71%. These results highlighted that the BCMSD plays significant roles in variations of aerosol optical properties and estimations of DARF as well as the air heating rate caused by the existence of BC particles. It was recommended that a real time measured BCMSD be used when estimating the aerosol DARF, instead of a constant one. The BCMSD was as important as that of the BC mixing states.

5 Conclusions

Knowledge of the BC microphysical properties especially the size-dependent information can help reduce the uncertainties when estimating the aerosol radiative effects. BCMSD is an important quantity in its own right, being directly and indirectly applicable to determination the sources, aging processes and mixing states of BC aerosols. In this study, the characteristics of BCMSD were studied from the field measurement results by using our own developed measurement algorithm.

The BCMSD measurement system was developed and validated based on the works of Ning et al. (2013) by using differential mobility analyzer (DMA) in tandem with Aethalometer (AE). When deriving the BCMSD, a comprehensive multiple charging correction algorithm was proposed and implied. This algorithm was validated by closure study between the measured total m_{BC} from AE33 and the m_{BC} integrated from the measured BC~~P~~MSD using the datasets from field measurements. Results showed that the multiple charging corrections could significantly change the shapes and magnitudes of the raw measured BC~~P~~MSD. The accurate BC~~P~~MSD characteristics could be obtained by our proposed method in this paper.

The developed measurement system was employed in a field campaign in the North China Plain from 21 Match to 9 April in 2017. The BCMSD was found to have two quasi-lognormal modes with peaks at around 150 nm and 500 nm, respectively. These two modes were consistent with the previous measurement results by MOUDI (Wang et al., 2015;Hu et al., 2012). The amount of the BC mass concentrations for the coarser mode peaks were about twice to that of the ~~fine~~ smaller mode.

The characteristic of the BCMSD was studied by fitting the shape of BCMSD with a bi-normal distribution. The relationships between the fitted D_m and GSD were statistically studied. During the aging processing, the opposite trends for the D_m and GSD were found for coarser mode. This is the first time that the coarser mode of the BCMSD were synthetically studied. The BCMSD of coarser mode varied significantly under different pollution conditions with peak diameter changed between 430 and 580 nm. However, the relationship between the D_m and GSD for smaller mode BC aerosols were more complex due to the complex sources.

When the BCMSD were changed with the polluted condition, the corresponding aerosol optical properties changes significantly. Sensitivity studies found that the aerosol g varies from 0.~~617~~ 603 to 0.~~649~~ 627 due to the variations in BCMSD. Aerosol g was more sensitive to D_m when the geometric mean diameter of the BCMSD is in the range of 300 nm and 370 nm. The SSA can changed from 0.90~~86~~ to 0.~~93~~94. The σ_{sca} experienced significant change with the variation of BCMSD from ~~264~~ 325.6 Mm^{-1} to ~~313~~ 364.4 Mm^{-1} and the σ_{abs} changed in the range between 2~~1.9~~4.064 Mm^{-1} and ~~44.12~~37.27 Mm^{-1}. The corresponding BC MAC was calculated to be in the range between ~~4.75~~5.44 and ~~9.56~~8.08 m^2/g.

The variations in DARF were estimated due to the variations of the BCMSD by using the SBDART model. Results showed that the DARF can varies by about ~~22.5~~8.45% for different BCMSD and the heating rate for different measured BCMSD conditions could change from ~~3.56~~2.24 to ~~3.75~~2.50, corresponding to a variation of ~~5.23~~11.6%. At the same time, the variations in DARF due to the variations in the BC mixing state was estimated to be ~~21.5~~10.5% and that of the heating rate is ~~6.05~~8.45%. Thus, the variations of the BCMSD may had significant influence on the aerosol radiative budget and an accurate measurement of BCMSD was very necessary.

Competing interests. The authors declare that they have no conflict of interest.

Data availability. The data used in this study is available when requesting the authors.

Author contributions. GZ, CZ, JT and YK designed and conducted the experiments; CS, YY, CZ and GZ discussed the results.

Acknowledgments. This work is supported by the National Key R&D Program of China (2016YFA0602001) and the National Natural Science Foundation of China (41590872).

References

Babu, S. S., Sreekanth, V., Moorthy, K. K., Mohan, M., Kirankumar, N. V. P., Subrahamanyam, D. B., Gogoi, M. M., Kompalli, S. K., Beegum, N., Chaubey, J. P., Kumar, V. H. A., and Manchandab, R. K.: Vertical profiles of aerosol black carbon in the atmospheric boundary layer over a tropical coastal station: Perturbations during an annular solar eclipse, Atmospheric Research, 99, 471-478, 10.1016/j.atmosres.2010.11.019, 2011.

Bau, S., Bemer, D., Grippari, F., Appert-Collin, J.-C., and Thomas, D.: Determining the effective density of airborne nanoparticles using multiple charging correction in a tandem DMA/ELPI setup, Journal of Nanoparticle Research, 16, 10.1007/s11051-014-2629-2, 2014.

Bohren, C. F., and Huffman, D. R.: Absorption and Scattering by a Sphere, in: Absorption and Scattering of Light by Small Particles, Wiley-VCH Verlag GmbH, 82-129, 2007.

Bond, T. C., Doherty, S. J., Fahey, D. W., Forster, P. M., Berntsen, T., DeAngelo, B. J., Flanner, M. G., Ghan, S., Karcher, B., Koch, D., Kinne, S., Kondo, Y., Quinn, P. K., Sarofim, M. C., Schultz, M. G., Schulz, M., Venkataraman, C., Zhang, H., Zhang, S., Bellouin, N., Guttikunda, S. K., Hopke, P. K., Jacobson, M. Z., Kaiser, J. W., Klimont, Z., Lohmann, U., Schwarz, J. P., Shindell, D., Storelvmo, T., Warren, S. G., and Zender, C. S.: Bounding the role of black carbon in the climate system: A scientific assessment, J Geophys Res-Atmos, 118, 5380-5552, 10.1002/jgrd.50171, 2013.

Cheng, Y. F., Su, H., Rose, D., Gunthe, S. S., Berghof, M., Wehner, B., Achtert, P., Nowak, A., Takegawa, N., Kondo, Y., Shiraiwa, M., Gong, Y. G., Shao, M., Hu, M., Zhu, T., Zhang, Y. H., Carmichael, G. R., Wiedensohler, A., Andreae, M. O., and Pöschl, U.: Size-resolved measurement of the mixing state of soot in the megacity Beijing, China: diurnal cycle, aging and parameterization, Atmospheric Chemistry and Physics, 12, 4477-4491, 10.5194/acp-12-4477-2012, 2012.

Cheng, Y. H., Liao, C. W., Liu, Z. S., Tsai, C. J., and Hsi, H. C.: A size-segregation method for monitoring the diurnal characteristics of atmospheric black carbon size distribution at urban traffic sites, Atmospheric Environment, 90, 78-86, 2014.

Cheng, Y. H., and Yang, L. S.: Characteristics of Ambient Black Carbon Mass and Size-Resolved Particle Number Concentrations during Corn Straw Open-Field Burning Episode Observations at a Rural Site in Southern Taiwan, Int J Environ Res Public Health, 13, 10.3390/ijerph13070688, 2016.

China, S., Mazzoleni, C., Gorkowski, K., Aiken, A. C., and Dubey, M. K.: Morphology and mixing state of individual freshly emitted wildfire carbonaceous particles, Nature communications, 4, 2122, 2013.

Deng, Z. Z., Zhao, C. S., Ma, N., Liu, P. F., Ran, L., Xu, W. Y., Chen, J., Liang, Z., Liang, S., Huang, M. Y., Ma, X. C., Zhang, Q., Quan, J. N., Yan, P., Henning, S., Mildenberger, K., Sommerhage, E., Schafer, M., Stratmann, F., and Wiedensohler, A.: Size-resolved and bulk activation properties of aerosols in the North China Plain, Atmospheric Chemistry and Physics, 11, 3835-3846, 10.5194/acp-11-3835-2011, 2011.

Drinovec, L., Močnik, G., Zotter, P., Prévôt, A. S. H., Ruckstuhl, C., Coz, E., Rupakheti, M., Sciare, J., Müller, T., Wiedensohler, A., and Hansen, A. D. A.: The "dual-spot" Aethalometer: an improved measurement of aerosol black carbon with real-time loading compensation, Atmospheric Measurement Techniques, 8, 1965-1979, 10.5194/amt-8-1965-2015, 2015.

Ferrero, L., Mocnik, G., Ferrini, B. S., Perrone, M. G., Sangiorgi, G., and Bolzacchini, E.: Vertical profiles of aerosol absorption coefficient from micro-Aethalometer data and Mie calculation over Milan, Science of the Total Environment, 409, 2824-2837, 10.1016/j.scitotenv.2011.04.022, 2011.

Gao, R. S., Schwarz, J. P., Kelly, K. K., Fahey, D. W., Watts, L. A., Thompson, T. L., Spackman, J. R., Slowik, J. G., Cross, E. S., Han, J. H., Davidovits, P., Onasch, T. B., and Worsnop, D. R.: A Novel Method for Estimating Light-Scattering Properties of Soot Aerosols Using a Modified Single-Particle Soot Photometer, Aerosol Sci. Technol., 41, 125-135, 10.1080/02786820601118398, 2007.

Gong, X., Zhang, C., Chen, H., Nizkorodov, S. A., Chen, J., and Yang, X.: Size distribution and mixing state of black carbon particles during a heavy air pollution episode in Shanghai, Atmos. Chem. Phys., 16, 5399-5411, 10.5194/acp-16-5399-2016, 2016.

Guo, Y.: Characteristics of size-segregated carbonaceous aerosols in the Beijing-Tianjin-Hebei region, Environ. Sci. Pollut. Res., 23, 13918-13930, 10.1007/s11356-016-6538-z, 2016.

Hagen, D. E., and Alofs, D. J.: Linear Inversion Method to Obtain Aerosol Size Distributions from Measurements with a Differential Mobility Analyzer, Aerosol Sci. Technol., 2, 465-475, 10.1080/02786828308958650, 2007.

Hansen, A. D. A., Rosen, H., and Novakov, T.: The aethalometer — An instrument for the real-time measurement of optical absorption by aerosol particles, Science of The Total Environment, 36, 191-196, http://dx.doi.org/10.1016/0048-9697(84)90265-1, 1984.

He, M., and Dhaniyala, S.: A multiple charging correction algorithm for scanning electrical mobility spectrometer data, Journal of Aerosol Science, 61, 13-26, 10.1016/j.jaerosci.2013.03.007, 2013.

He, M., Dhaniyala, S., and Wagner, M.: Aerosol Filtration with Mobility-Classified Particles: Role of Multiply Charged Particles in Skewing Penetration Measurements, Aerosol Sci. Technol., 49, 704-715, 10.1080/02786826.2015.1062467, 2015.

Hu, M., Peng, J., Sun, K., Yue, D., Guo, S., Wiedensohler, A., and Wu, Z.: Estimation of size-resolved ambient particle density based on the measurement of aerosol number, mass, and chemical size distributions in the winter in Beijing, Environ Sci Technol, 46, 9941-9947, 10.1021/es204073t, 2012.

Huang, X.-F., Sun, T.-L., Zeng, L.-W., Yu, G.-H., and Luan, S.-J.: Black carbon aerosol characterization in a coastal city in South China using a single particle soot photometer, Atmospheric Environment, 51, 21-28, 10.1016/j.atmosenv.2012.01.056, 2012.

Huang, X. F., and Yu, J. Z.: Size distributions of elemental carbon in the atmosphere of a coastal urban area in South China: characteristics, evolution processes, and implications for the mixing state, Atmospheric Chemistry and Physics, 8, 5843-5853, 2008.

Jacobson, M. Z.: Strong radiative heating due to the mixing state of black carbon in atmospheric aerosols, Nature, 409, 695-697, 2001.

Janssen, N. A. H., Hoek, G., Simic-Lawson, M., Fischer, P., van Bree, L., ten Brink, H., Keuken, M., Atkinson, R. W., Anderson, H. R., Brunekreef, B., and Cassee, F. R.: Black Carbon as an Additional Indicator of the Adverse Health Effects of Airborne Particles Compared with PM10 and PM2.5, Environ Health Persp, 119, 1691-1699, 10.1289/ehp.1003369, 2011.

KlausWilleke, and Baron, P.: Aerosol measurement : principles, techniques, and applications, Van Nostrand Reinhold, 807-808 pp., 1996.

Knutson, E. O., and Whitby, K. T.: Aerosol classification by electric mobility: apparatus, theory, and applications, Journal of Aerosol Science, 6, 443-451, 1975.

Koch, D., Schulz, M., Kinne, S., and Mcnaughton, C.: Evaluation of black carbon estimations in global aerosol models, Atmospheric Chemistry & Physics, 9, 9001-9026, 2009.

Koch, D., and Del Genio, A. D.: Black carbon semi-direct effects on cloud cover: review and synthesis, Atmos. Chem. Phys., 10, 7685-7696, 10.5194/acp-10-7685-2010, 2010.

Kuang, Y., Zhao, C. S., Tao, J. C., and Ma, N.: Diurnal variations of aerosol optical properties in the North China Plain and their influences on the estimates of direct aerosol radiative effect, Atmos. Chem. Phys., 15, 5761-5772, 10.5194/acp-15-5761-2015, 2015.

Kuang, Y., Zhao, C. S., Tao, J. C., Bian, Y. X., and Ma, N.: Impact of aerosol hygroscopic growth on the direct aerosol radiative effect in summer on North China Plain, Atmospheric Environment, 147, 224-233, 2016.

Lippmann, M., and Albert, R. E.: The Effect of Particle Size on the Regional Deposition of Inhaled Aerosols in the Human Respiratory Tract, American Industrial Hygiene Association Journal, 30, 257-275, 10.1080/00028896909343120, 1969.

Liu, D., Whitehead, J., Alfarra, M. R., Reyes-Villegas, E., Spracklen, Dominick V., Reddington, Carly L., Kong, S., Williams, Paul I., Ting, Y.-C., Haslett, S., Taylor, Jonathan W., Flynn, Michael J., Morgan, William T., McFiggans, G., Coe, H., and Allan, James D.: Black-carbon absorption enhancement in the atmosphere determined by particle mixing state, Nature Geoscience, 10, 184-188, 10.1038/ngeo2901, 2017.

Ma, N., Zhao, C. S., Müller, T., Cheng, Y. F., Liu, P. F., Deng, Z. Z., Xu, W. Y., Ran, L., Nekat, B., van Pinxteren, D., Gnauk, T., Müller, K., Herrmann, H., Yan, P., Zhou, X. J., and Wiedensohler, A.: A new method to determine the mixing state of light absorbing carbonaceous using the measured aerosol optical properties and number size distributions, Atmos. Chem. Phys., 12, 2381-2397, 10.5194/acp-12-2381-2012, 2012.

Matsui, H., Hamilton, D. S., and Mahowald, N. M.: Black carbon radiative effects highly sensitive to emitted particle size when resolving mixing-state diversity, Nature communications, 9, 3446, 10.1038/s41467-018-05635-1, 2018.

Menon, S., Hansen, J., Nazarenko, L., and Luo, Y.: Climate effects of black carbon aerosols in China and India, Science, 297, 2250-2253, 10.1126/science.1075159, 2002.

Moffet, R. C., amp, apos, Brien, R. E., Alpert, P. A., Kelly, S. T., Pham, D. Q., Gilles, M. K., Knopf, D. A., and Laskin, A.: Morphology and mixing of black carbon particles collected in central California during the CARES field study, Atmospheric Chemistry and Physics, 16, 14515-14525, 10.5194/acp-16-14515-2016, 2016.

Moteki, N., and Kondo, Y.: Dependence of Laser-Induced Incandescence on Physical Properties of Black Carbon Aerosols: Measurements and Theoretical Interpretation, Aerosol Sci. Technol., 44,

663-675, Pii 924375405
10.1080/02786826.2010.484450, 2010.

Nichols, J. L., Owens, E. O., Dutton, S. J., and Luben, T. J.: Systematic review of the effects of black carbon on cardiovascular disease among individuals with pre-existing disease, International Journal of Public Health, 58, 707-724, 2013.

Ning, Z., Chan, K. L., Wong, K. C., Westerdahl, D., Močnik, G., Zhou, J. H., and Cheung, C. S.: Black carbon mass size distributions of diesel exhaust and urban aerosols measured using differential mobility analyzer in tandem with Aethalometer, Atmospheric Environment, 80, 31-40, 10.1016/j.atmosenv.2013.07.037, 2013.

Ohata, S., Moteki, N., and Kondo, Y.: Evaluation of a Method for Measurement of the Concentration and Size Distribution of Black Carbon Particles Suspended in Rainwater, Aerosol Sci. Technol., 45, 1326-1336, 2011.

Peng, J., Hu, M., Guo, S., Du, Z., Zheng, J., Shang, D., Levy Zamora, M., Zeng, L., Shao, M., Wu, Y.-S., Zheng, J., Wang, Y., Glen, C. R., Collins, D. R., Molina, M. J., and Zhang, R.: Markedly enhanced absorption and direct radiative forcing of black carbon under polluted urban environments, Proceedings of the National Academy of Sciences, 201602310, 10.1073/pnas.1602310113, 2016.

Peng, J., Hu, M., Guo, S., Du, Z., Shang, D., Zheng, J., Zheng, J., Zeng, L., Shao, M., Wu, Y., Collins, D., and Zhang, R.: Ageing and hygroscopicity variation of black carbon particles in Beijing measured by a quasi-atmospheric aerosol evolution study (QUALITY) chamber, Atmospheric Chemistry and Physics, 17, 10333-10348, 10.5194/acp-17-10333-2017, 2017.

Raatikainen, T., Brus, D., Hooda, R. K., Hyvärinen, A.-P., Asmi, E., Sharma, V. P., Arola, A., and Lihavainen, H.: Size-selected black carbon mass distributions and mixing state in polluted and clean environments of northern India, Atmospheric Chemistry and Physics, 17, 371-383, 10.5194/acp-17-371-2017, 2017.

Ramachandran, S., and Rajesh, T. A.: Black carbon aerosol mass concentrations over Ahmedabad, an urban location in western India: Comparison with urban sites in Asia, Europe, Canada, and the United States, J Geophys Res-Atmos, 112, Artn D06211
10.1029/2006jd007488, 2007.

Ramanathan, V., and Carmichael, G.: Global and regional climate changes due to black carbon, Nature Geoscience, 1, 221-227, 10.1038/ngeo156, 2008.

Ran, L., Deng, Z., Xu, X., Yan, P., Lin, W., Wang, Y., Tian, P., Wang, P., Pan, W., and Lu, D.: Vertical profiles of black carbon measured by a micro-aethalometer in summer in the North China Plain, Atmospheric Chemistry and Physics, 16, 10441-10454, 10.5194/acp-16-10441-2016, 2016a.

Ran, L., Deng, Z. Z., Wang, P. C., and Xia, X. A.: Black carbon and wavelength-dependent aerosol absorption in the North China Plain based on two-year aethalometer measurements, Atmospheric Environment, 142, 132-144, 10.1016/j.atmosenv.2016.07.014, 2016b.

Reddington, C. L., McMeeking, G., Mann, G. W., Coe, H., Frontoso, M. G., Liu, D., Flynn, M., Spracklen, D. V., and Carslaw, K. S.: The mass and number size distributions of black carbon aerosol over Europe, Atmospheric Chemistry and Physics, 13, 4917-4939, 10.5194/acp-13-4917-2013, 2013.

Ricchiazzi, P., Yang, S., Gautier, C., and Sowle, D.: SBDART: A Research and Teaching Software Tool for Plane-Parallel Radiative Transfer in the Earth's Atmosphere, Bulletin of the American Meteorological Society, 79, 2101-2114, 10.1175/1520-0477(1998)079<2101:sarats>2.0.co;2, 1998.

Roberts, G. C., Ramana, M. V., Corrigan, C., Kim, D., and Ramanathan, V.: Simultaneous observations of aerosol-cloud-albedo interactions with three stacked unmanned aerial vehicles, Proceedings of the National Academy of Sciences of the United States of America, 105, 7370-7375, 10.1073/pnas.0710308105, 2008.

Schwarz, J. P., Gao, R. S., Fahey, D. W., Thomson, D. S., Watts, L. A., Wilson, J. C., Reeves, J. M., Darbeheshti, M., Baumgardner, D. G., Kok, G. L., Chung, S. H., Schulz, M., Hendricks, J., Lauer, A., Kärcher, B., Slowik, J. G., Rosenlof, K. H., Thompson, T. L., Langford, A. O., Loewenstein, M., and Aikin, K. C.: Single-particle measurements of midlatitude black carbon and light-scattering aerosols from the boundary layer to the lower stratosphere, Journal of Geophysical Research, 111, 10.1029/2006jd007076, 2006.

Singh, S., Fiddler, M. N., and Bililign, S.: Measurement of size-dependent single scattering albedo of fresh biomass burning aerosols using the extinction-minus-scattering technique with a combination of cavity ring-down spectroscopy and nephelometry, Atmospheric Chemistry and Physics, 16, 13491-13507, 10.5194/acp-16-13491-2016, 2016.

Song, S., Wu, Y., Xu, J., Ohara, T., Hasegawa, S., Li, J., Yang, L., and Hao, J.: Black carbon at a roadside site in Beijing: Temporal variations and relationships with carbon monoxide and particle number size distribution, Atmospheric Environment, 77, 213-221, https://doi.org/10.1016/j.atmosenv.2013.04.055, 2013.

Stabile, L., Fuoco, F. C., and Buonanno, G.: Characteristics of particles and black carbon emitted by combustion of incenses, candles and anti-mosquito products, Building and Environment, 56, 184-191, 10.1016/j.buildenv.2012.03.005, 2012.

Stevens, B., and Feingold, G.: Untangling aerosol effects on clouds and precipitation in a buffered system, Nature, 461, 607-613, 10.1038/nature08281, 2009.

Tigges, L., Wiedensohler, A., Weinhold, K., Gandhi, J., and Schmid, H. J.: Bipolar charge distribution of a soft X-ray diffusion charger, Journal of Aerosol Science, 90, 77-86, 10.1016/j.jaerosci.2015.07.002, 2015.

Turner, M. D., Henze, D. K., Hakami, A., Zhao, S. L., Resler, J., Carmichael, G. R., Stanier, C. O., Baek, J., Sandu, A., Russell, A. G., Nenes, A., Jeong, G. R., Capps, S. L., Percell, P. B., Pinder, R. W., Napelenok, S. L., Bash, J. O., and Chai, T. F.: Differences Between Magnitudes and Health Impacts of BC Emissions Across the United States Using 12 km Scale Seasonal Source Apportionment, Environmental Science & Technology, 49, 4362-4371, 10.1021/es505968b, 2015.

Venkataraman, C., and Friedlander, S. K.: Size distributions of polycyclic aromatic hydrocarbons and elemental carbon. 2. Ambient measurements and effects of atmospheric processes, Environmental Science & Technology, 28, 563, 1994.

Virkkula, A., Makela, T., Hillamo, R., Yli-Tuomi, T., Hirsikko, A., Hameri, K., and Koponen, I. K.: A simple procedure for correcting loading effects of aethalometer data, J Air Waste Manag Assoc, 57, 1214-1222, 10.3155/1047-3289.57.10.1214, 2007.

Virkkula, A., Chi, X., Ding, A., Shen, Y., Nie, W., Qi, X., Zheng, L., Huang, X., Xie, Y., Wang, J., Petaja, T., and Kulmala, M.: On the interpretation of the loading correction of the aethalometer, Atmospheric Measurement Techniques, 8, 4415-4427, 10.5194/amt-8-4415-2015, 2015.

Wang, Q. Y., Huang, R. J., Cao, J. J., Tie, X. X., Ni, H. Y., Zhou, Y. Q., Han, Y. M., Hu, T. F., Zhu, C. S., Feng, T., Li, N., and Li, J. D.: Black carbon aerosol in winter northeastern Qinghai–Tibetan Plateau, China: the source, mixing state and optical property, Atmospheric Chemistry and Physics, 15, 13059-13069, 10.5194/acp-15-13059-2015, 2015.

Wex, H., Neusüß, C., Wendisch, M., Stratmann, F., Koziar, C., Keil, A., Wiedensohler, A., and Ebert, M.: Particle scattering, backscattering, and absorption coefficients: An in situ closure and sensitivity study, Journal of Geophysical Research: Atmospheres, 107, LAC 4-1-LAC 4-18, 10.1029/2000jd000234, 2002.

Wiedensohler, A.: An approximation of the bipolar charge distribution for particles in the submicron size range, Journal of Aerosol Science, 19, 387-389, 1988.

Wiedensohler, A., and Fissan, H. J.: Aerosol charging in high purity gases, Journal of Aerosol Science, 19, 867-870, 1988.

Wilcox, E. M., Thomas, R. M., Praveen, P. S., Pistone, K., Bender, F. A. M., and Ramanathan, V.: Black carbon solar absorption suppresses turbulence in the atmospheric boundary layer, Proceedings of the National Academy of Sciences, 113, 11794-11799, 10.1073/pnas.1525746113, 2016.

Wu, Y., Cheng, T., Zheng, L., and Chen, H.: Effect of morphology on the optical properties of soot aggregated with spheroidal monomers, Journal of Quantitative Spectroscopy & Radiative Transfer, 168, 158-169, 2016a.

Wu, Y., Wang, X., Tao, J., Huang, R., Tian, P., Cao, J., Zhang, L., Ho, K.-F., and Zhang, R.: Size distribution and source of black carbon aerosol in urban Beijing during winter haze episodes, Atmospheric Chemistry and Physics Discussions, 1-25, 10.5194/acp-2016-1096, 2016b.

Wu, Y., Cheng, T., Liu, D., Allan, J. D., Zheng, L., and Chen, H.: Light Absorption Enhancement of Black Carbon Aerosol Constrained by Particle Morphology, Environ Sci Technol, 52, 6912-6919, 10.1021/acs.est.8b00636, 2018.

Yu, H., and Yu, J. Z.: Modal Characteristics of Elemental and Organic Carbon in an Urban Location in Guangzhou, China, Aerosol Sci. Technol., 43, 1108-1118, 2009.

Yu, H., Wu, C., Wu, D., and Yu, J. Z.: Size distributions of elemental carbon and its contribution to light extinction in urban and rural locations in the pearl river delta region, China, Atmos. Chem. Phys., 10, 5107-5119, 10.5194/acp-10-5107-2010, 2010.

Zhang, R., Khalizov, A. F., Pagels, J., Zhang, D., Xue, H., and McMurry, P. H.: Variability in morphology, hygroscopicity, and optical properties of soot aerosols during atmospheric processing, Proceedings of the National Academy of Sciences of the United States of America, 105, 10291-10296, 10.1073/pnas.0804860105, 2008.

Zhang, Y., Zhang, Q., Cheng, Y., Su, H., Kecorius, S., Wang, Z., Wu, Z., Hu, M., Zhu, T., Wiedensohler, A., and He, K.: Measuring the morphology and density of internally mixed black carbon with SP2 and VTDMA: new insight into the absorption enhancement of black carbon in the atmosphere, Atmospheric Measurement Techniques, 9, 1833-1843, 10.5194/amt-9-1833-2016, 2016.

Zhang, Y., Su, H., Kecorius, S., Wang, Z., Hu, M., Zhu, T., He, K., Wiedensohler, A., Zhang, Q., and Cheng, Y.: Mixing State of Refractory Black Carbon of the North China Plain Regional Aerosol Combining a Single Particle Soot Photometer and a Volatility Tandem Differential Mobility Analyzer, Atmospheric Chemistry and Physics Discussions, 1-27, 10.5194/acp-2017-222, 2017.

Zhang, Y., Zhang, Q., Cheng, Y., Su, H., Li, H., Li, M., Zhang, X., Ding, A., and He, K.: Amplification of light absorption of black carbon associated with air pollution, Atmospheric Chemistry and Physics, 18, 9879-9896, 10.5194/acp-18-9879-2018, 2018.

Zhao, G., Zhao, C., Kuang, Y., Bian, Y., Tao, J., Shen, C., and Yu, Y.: Calculating the aerosol asymmetry factor based on measurements from the humidified nephelometer system, Atmospheric Chemistry and Physics, 18, 9049-9060, 10.5194/acp-18-9049-2018, 2018.

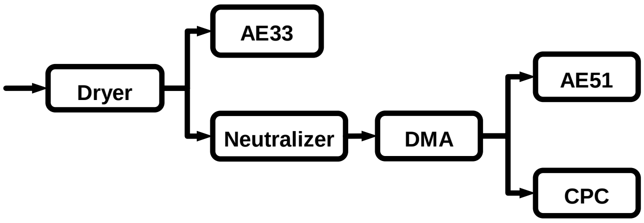

Figure 1. The schematic diagram of the instrument setup.

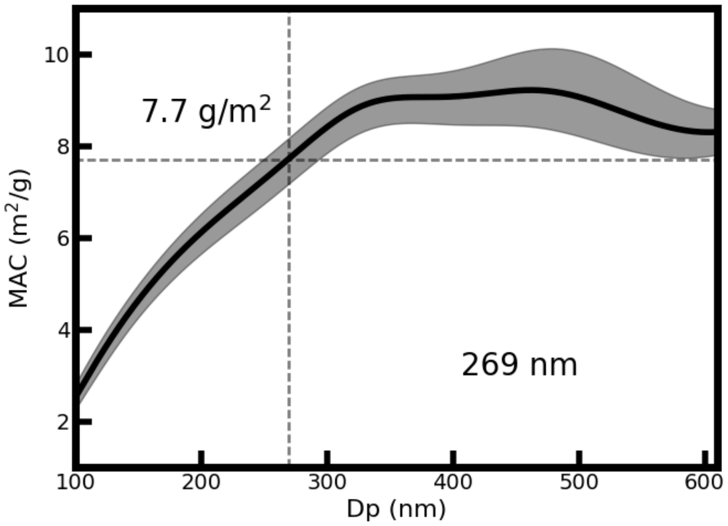

Figure 2. Calculated mass absorption coefficient of different aerosol.

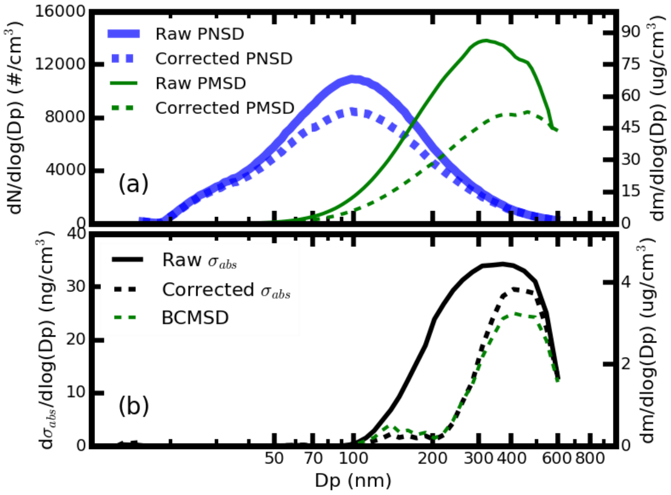

Figure ~~2~~3. Case of multiple charging correction processing. (a) the multiple charging correction of the aerosol PNSD and aerosol PMSD, (b) the multiple charging correction of the size-resolved σ_{abs}~~the BCPMSD~~. The solid line is the measured results without multiple charging corrections and the dotted line is the multiple charging corrections results.

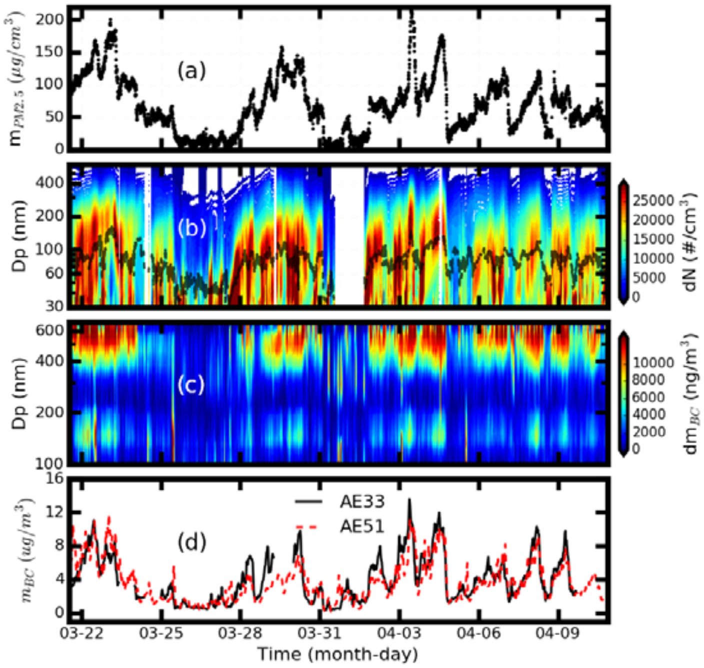

Figure ~~3~~4. The measured time series of mass concentrations for (a) the PM2.5; (b) the aerosol PNSD in filled color, the geometric median diameter in dotted line; ~~and~~ (c) the BCMSD and~~.~~ (d) the m_{BC} by AE33 (black) and m_{BC} from integrated BCMSD from AE51 (red).

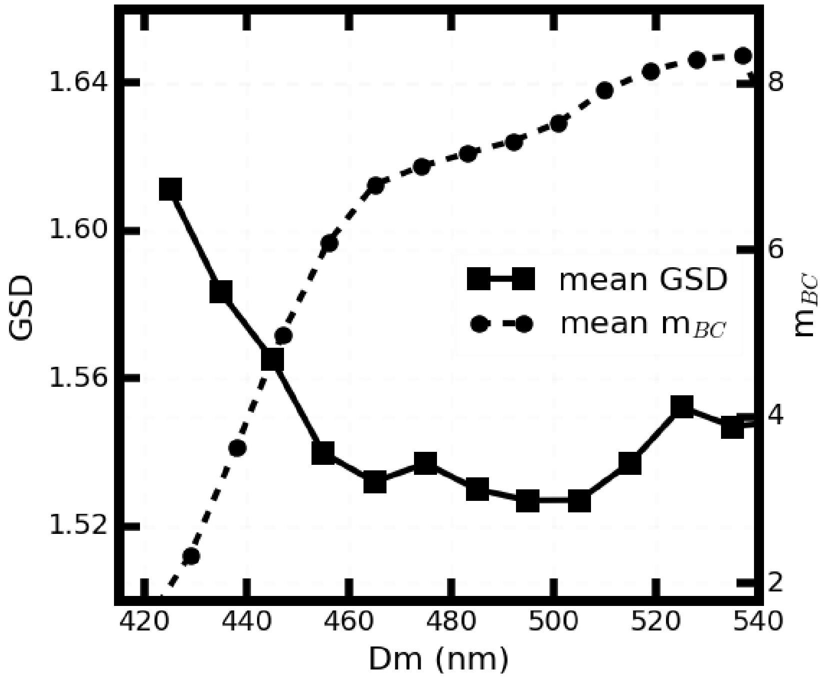

Figure 5. The relationship between the Dm and the GSD. The black dots show the real measured Dm and GSD. The black line shows the mean results of the GSD for different Dm. The black line marked with square shows the variation of mean m_{BC} with the Dm.

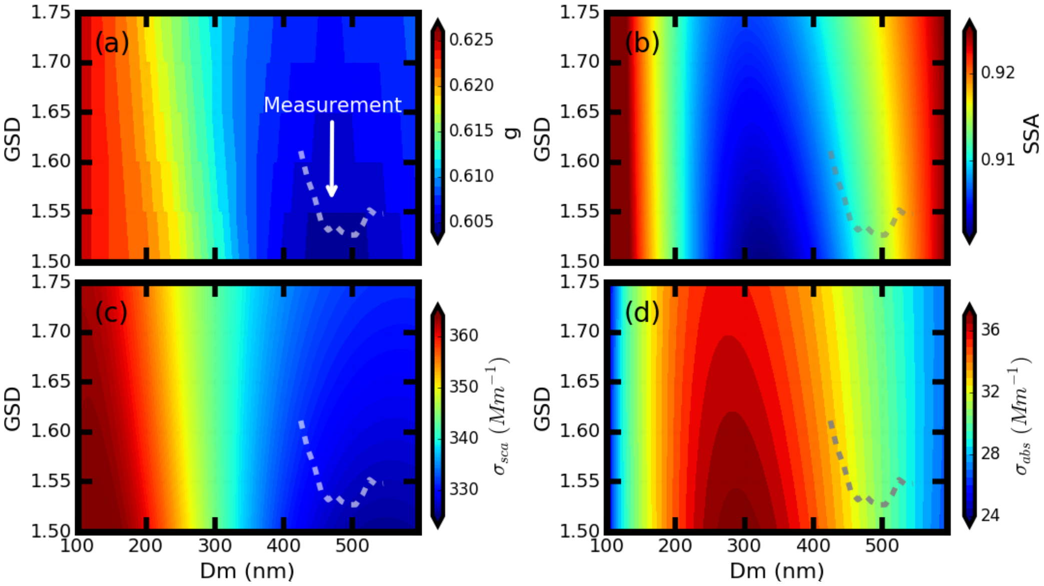

Figure 6. Variations of aerosol optics properties using the measured mean aerosol PNSD and m_{BC} under different BCMSD conditions, which are represented by different Dm and GSD values: (a) aerosol asymmetry factor, (b) single scatter albedo, (c) scattering coefficient and (d) extinction coefficient . The grey dotted line in the figure shows the evolution path of the BCMSD according to results of field measurements.

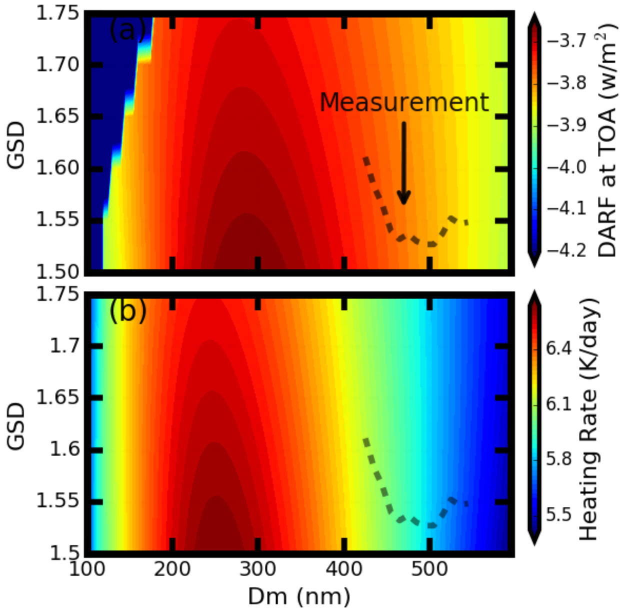

Figure 7. Variations of (a) DARF and (b) heating rate under different BCMSD conditions, which are represented by different Dm and GSD values. The black dotted line in the figure shows the evolution path of the BCMSD according to results of field measurements.

Table 1. Comparison of the DARF and heating rate values under different BC mixing states and different BCMSD conditions.

		Mixing State			**BCMSD**	
		Internal	**External**	**Core-Shell**	**Minimum**	**Maximum**
DARF	**Value(w/m^2)**	**-3.45**	**-3.56**	**-3.81**	**-3.97**	**-3.67**
	Variation	**10.5%**			**8.45%**	
Heat Rate	**Value(K/day)**	**2.51**	**2.32**	**2.53**	**2.24**	**2.50**
	Variation	**9.71%**			**11.6%**	

Supplement for

Role of black carbons mass size distribution in the direct aerosol radiative forcing

Gang Zhao[1], Jiangchuan Tao[2], Ye Kuang[2], Chuanyang Shen[1], Yingli Yu[1], Chunsheng Zhao[1*]

1 Department of Atmospheric and Oceanic Sciences, School of Physics, Peking University, 100871 Beijing, China

2 Institute for Environmental and Climate Research, Jinan University, 511443 Guangzhou, China

1. Correcting the AE51

Fig. S1 showed the results of the loading effect corrections. At the beginning of the field experiment, parallel measurement of σ_{abs} by AE51 and AE33 was conducted. Before corrections, the measured σ_{abs} by AE51 and AE33 showed significant discrepancy with each other with slope and R^2 equaling 0.55 and 0.83. However, the σ_{abs} measured by AE33 and by AE51 with loading effects corrections showed good consistency in trends and magnitudes with slope and R^2 of 0.98 and 0.94 respectively. These results demonstrated that the loading effects corrections of σ_{abs} from AE51 were essential and the value of σ_{abs} from AE33 can be used as a reference for the measured size-resolved σ_{abs}.

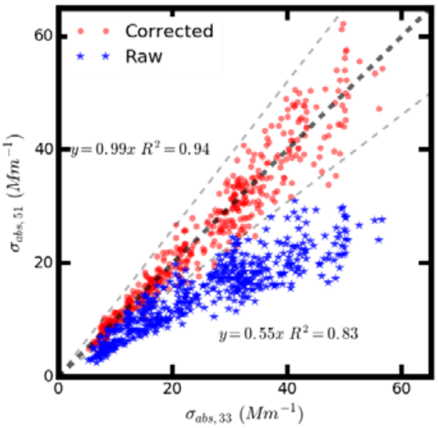

Figure S1. Comparison between the σ_{abs} measured by AE51 and AE33. The blue stars and the red dots represents uncorrected and corrected σ_{abs} of AE51 respectively.

2. Time correction

There were two reasons that can lead to this difference: firstly, the time of the AE51 system and the computer that controls the CPC cannot be synchronized all the time; secondly, there existed a difference in the plumbing delay time, which was the time required for particles to flow through the tubing interconnecting the DMA and CPC or AE51, and arrive at the detector. To sum up, the synchronization of the time reported by CPC and AE51 was necessary.

Time synchronization was conducted by measuring the time lag of the signal pulses from the DMA to CPC and AE51. The signal pulses resulted from the sudden change of the aerosol diameter scanned by DMA. Details of the method were shown below. In fig. S2, the black solid line gave the time series of the measured σ_{abs} by AE51. The dotted lines gave the time series of the aerosol number counted by CPC of (a) unsynchronized and (b) synchronized. In the beginning, the scan diameter of the DMA was set to be less than 13nm and the values measured by AE51 and CPC are nearly zero. The values get a step jump and a step drop when changing the scan diameter up to about 200nm and down back to less than 13nm. About 15s later, these procedures were conducted once again. From fig. S2(a) and fig. S2(b), the lag time of the AE51 and CPC were determined to be 20s by matching the pulse signals.

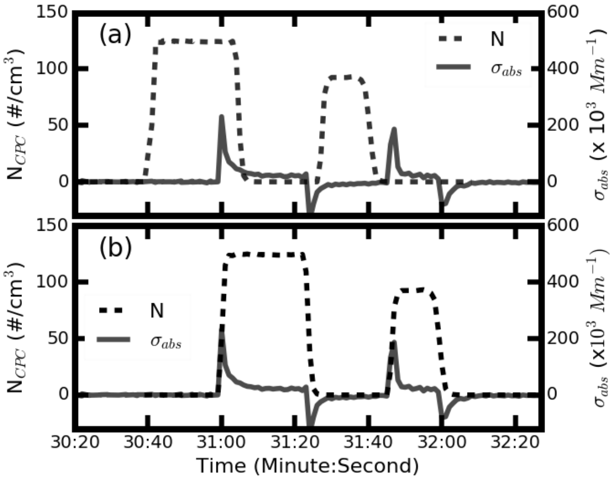

Figure S2. An example of time synchronization processing, (a) for unsynchronized and (b) for synchronized. The dotted line is the aerosol number concentration time series counted by CPC. The black solid line is the σ_{abs} measured by AE51.

3. Time series diagram of scanned aerosol diameters, measured m_{BC} and the aerosol number

concentrations

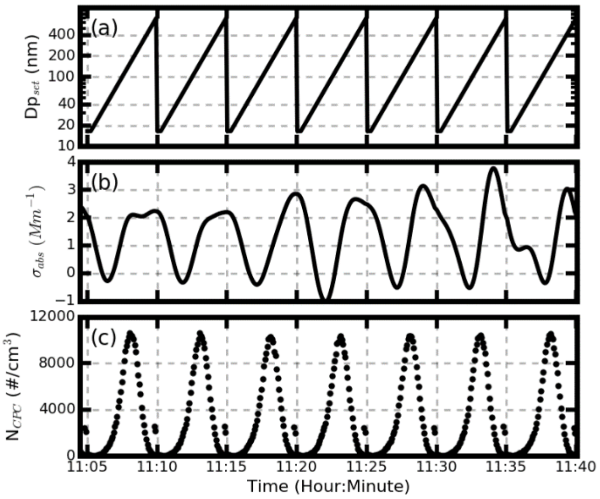

Figure S3 (a) the diameters of the aerosols that pass through the DMA (b) The σ_{abs} values measured by AE51, (c) the aerosol number concentrations measured by CPC.

4 Validation of the multiple charging corrections

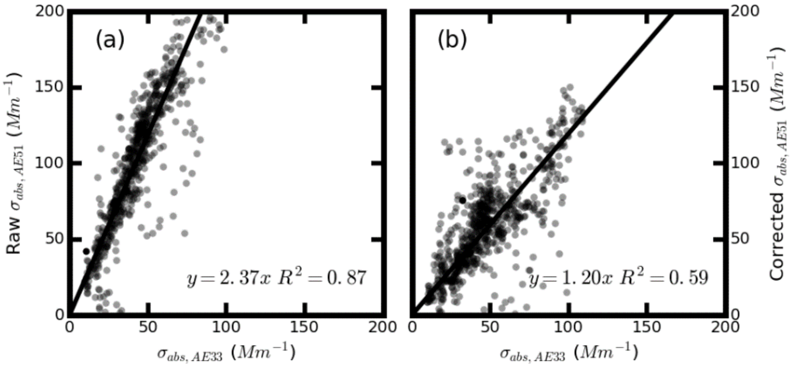

Figure S4. σ_{abs} measured by AE33 versus σ_{abs} integrated from AE51 of (a) uncorrected size-resolved σ_{abs}, (b) multiple-charging corrected size-resolved σ_{abs}.

5 Estimate the DARF

DARF is defined as the difference between radiative flux at the TOA under present aerosol conditions and aerosol-free conditions:

$$\mathrm{DARF} = (f_a \downarrow - f_a \uparrow) - (f_m \downarrow - f_m \uparrow) \ , \qquad (21)$$

Where $f_a \downarrow$ is the downward radiative irradiance and $f_a \uparrow$ is the outward radiative irradiance under given aerosol distributions; $(f_a \downarrow - f_a \uparrow)$ is the downward radiative irradiance flux with given aerosol distributions and $(f_m \downarrow - f_m \uparrow)$ is the radiative irradiance flux under aerosol free conditions.

Input data for the SBDART are listed below. Vertical profiles of the aerosol optical properties, which include the aerosol extinction coefficient (σ_{ext}), aerosol single scattering albedo (SSA) and g with a height resolution of 50 m, come from the parameterization of aerosol vertical distributions (as shown in fig. S4 and the next paragraph) and the results of the Mie model. Atmospheric gas and meteorological parameter profiles come from the mean results of the radiosonde observations at the Meteorological Bureau of Beijing (39°48' N, 116°28' E), which include profiles for water vapor, pressure and temperature during the spring. Surface albedo values are obtained from the Moderate Resolution Imaging Spectroradiometer (MODIS) V005 Climate Modeling Grid (CMG) Albedo Product (MCD43C3) during March, 2017 of Beijing, where the field campaign is conducted. The remaining input data for the SBDART are set to their default values.

5.1 Parameterization of the aerosol vertical distribution

Liu et al. (2009) studied vertical profiles of aerosol total number concentration (Na) with aircraft measurements, and derived a parameterized vertical distribution. In this scheme, Na is constant in the mixed layer, with a transition layer where it linearly decreases and an exponential decrease of Na above the transition layer. The same parameterized scheme proposed by Liu et al. (2009) is adopted by this study as shown in fig. S4 (b). Both the study of Liu et al. (2009) and Ferrero et al. (2010) manifest that the dry aerosol PNSD in the mixed layer varies little. The shape of the dry aerosol PNSD is assumed constant with height, which means that aerosol PNSD at different heights divided by Na give the same normalized PNSD.

As for the BC vertical distribution, Ferrero et al. (2011) and Ran et al. (2016) demonstrate that BC mass concentration in the mixed layer remains relatively constant and decreases sharply above the mixed layer. According to this, the parameterization scheme of BC vertical distribution is assumed to be the same as that of aerosol. The shape of the size-resolved BC mass concentration distribution is also assumed to be the same as that at the surface.

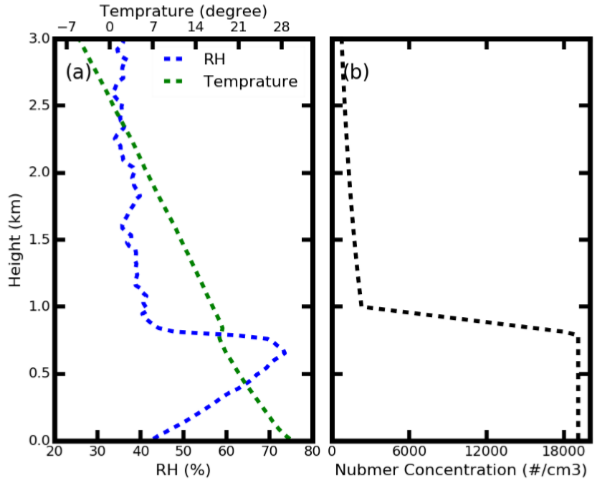

Figure S5. The mean RH, temperature, and aerosol number concentration profiles.

5.2 Calculate the aerosol optical profiles under the given RH profile

With the vertical distribution of aerosol PNSD and BCMSD, the aerosol optical properties at a given RH profile can be calculated by using the Mie scattering model and κ-Köhler theory (Petters and Kreidenweis, 2007).

The aerosol hygroscopic growth is taken into consideration when calculate the aerosol optical properties under the given RH. The κ-Köhler theory (Petters and Kreidenweis, 2007) is widely used to describe the hygroscopic growth of aerosol particles by using a single aerosol hygroscopic growth parameter (κ) and the κ-Köhler equation, which is shown as

$$\frac{RH}{100} = \frac{gf^3-1}{gf^3-(1-\kappa)} \cdot \exp\left(\frac{4\sigma_{s/a}M_{water}}{R\cdot T\cdot D_d\cdot gf\cdot \rho_w}\right) , \quad (1)$$

where D_d is the dry particle diameter; gf(RH) is the aerosol growth factor, which is defined as the ratio of the aerosol diameter at a given RH and the dry aerosol diameter (D_{RH}/D_d); T is the temperature; $\sigma_{s/a}$ is the surface tension of the solution; R is the universal gas constant and ρ_w is the density of water. The aerosol hygroscopic growth parameter κ can be further used to investigate the influence of aerosol hygroscopic growth on aerosol optical properties (Tao et al., 2014;Kuang et al., 2015;Zhao et al., 2017) and aerosol liquids water contents (Bian et al., 2014).

The κ-Köhler theory and the Mie scattering model are combined to calculate aerosol extinction coefficient, aerosol single scattering albedo and aerosol asymmetry factor under different RH conditions. The measured mean κ, which is derived from the humidified nephelometer system (Kuang et al., 2017), is used to account for aerosol hygroscopic growth. For each RH value, the gf can be calculated based on equation (1). The corresponding ambient aerosol PNSD at a given RH can be determined. The refractive index ($\widetilde{m}$), which accounts for water content in the particle, is derived as a volume mixture between the dry aerosol and water (Wex et al., 2002):

$$\widetilde{m} = f_{V,dry}\,\widetilde{m}_{aero,dry} + (1 - f_{V,dry})\,\widetilde{m}_{water} \qquad (2)$$

where $f_{v,dry}$ is the ratio of the dry aerosol volume to the total aerosol volume under a given RH condition; $\widetilde{m}_{aero,dry}$ is the refractive index for dry ambient aerosols and $\widetilde{m}_{water}$, the refractive index of water, is $1.33+10^{-7}i$. Then, the corresponding aerosol optical properties under the given RH and PNSD can also be calculated. Finally, the aerosol optical profiles can be calculated. Fig. S6 shows one of the calculated aerosol optical profiles.

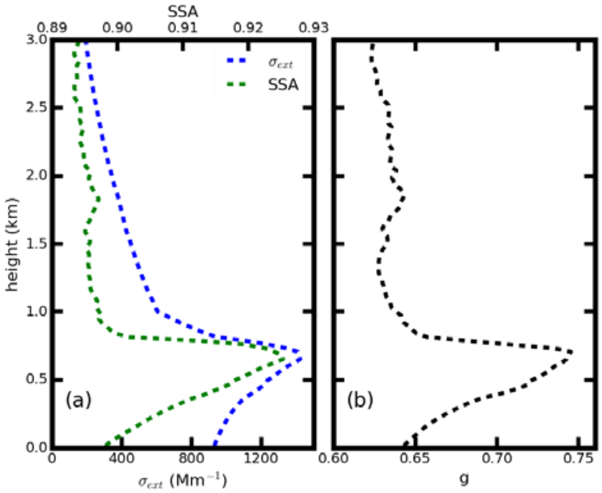

Figure S6. The calculated profiles of the aerosol extinction coefficient, aerosol single scattering albedo and the aerosol asymmetry factor.

6 Relationship between the GSD, Dm and m_{BC}

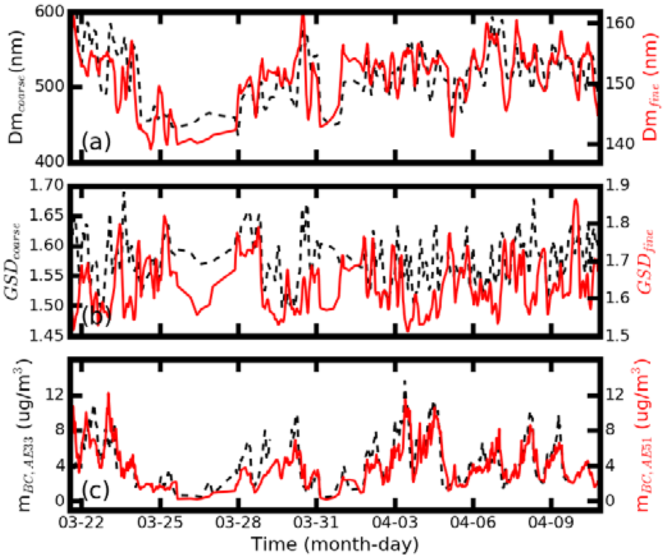

Figure S7. The (a) Dm and (b) GSD of the BCMSD at coarse mode (black) and fine mode (red); (c) measured m_{BC} by AE33 (black) and measured m_{BC} from integrated m_{BC} of the BCMSD from AE51.

Bian, Y. X., Zhao, C. S., Ma, N., Chen, J., and Xu, W. Y.: A study of aerosol liquid water content based on hygroscopicity measurements at high relative humidity in the North China Plain, Atmospheric Chemistry and Physics, 14, 6417-6426, 10.5194/acp-14-6417-2014, 2014.

Ferrero, L., Perrone, M. G., Petraccone, S., Sangiorgi, G., Ferrini, B. S., Lo Porto, C., Lazzati, Z., Cocchi, D., Bruno, F., Greco, F., Riccio, A., and Bolzacchini, E.: Vertically-resolved particle size distribution within and above the mixing layer over the Milan metropolitan area, Atmospheric Chemistry and Physics, 10, 3915-3932, 2010.

Ferrero, L., Mocnik, G., Ferrini, B. S., Perrone, M. G., Sangiorgi, G., and Bolzacchini, E.: Vertical profiles of aerosol absorption coefficient from micro-Aethalometer data and Mie calculation over Milan, Science of the Total Environment, 409, 2824-2837, 2011.

Kuang, Y., Zhao, C. S., Tao, J. C., and Ma, N.: Diurnal variations of aerosol optical properties in the North China Plain and their influences on the estimates of direct aerosol radiative effect, Atmos. Chem. Phys., 15, 5761-5772, 10.5194/acp-15-5761-2015, 2015.

Kuang, Y., Zhao, C., Tao, J., Bian, Y., Ma, N., and Zhao, G.: A novel method for deriving the aerosol hygroscopicity parameter based only on measurements from a humidified nephelometer system, Atmos. Chem. Phys., 17, 6651-6662, 10.5194/acp-17-6651-2017, 2017.

Liu, P., Zhao, C., Zhang, Q., Deng, Z., Huang, M., Xincheng, M. A., and Tie, X.: Aircraft study of aerosol vertical distributions over Beijing and their optical properties, Tellus Series B-Chemical & Physical Meteorology, 61, 756–767, 2009.

Petters, M. D., and Kreidenweis, S. M.: A single parameter representation of hygroscopic growth and cloud condensation nucleus activity, Atmos. Chem. Phys., 7, 1961-1971, 10.5194/acp-7-1961-2007, 2007.

Ran, L., Deng, Z., Xu, X., Yan, P., Lin, W., Wang, Y., Tian, P., Wang, P., Pan, W., and Lu, D.: Vertical profiles of black carbon measured by a micro-aethalometer in summer in the North China Plain, Atmospheric Chemistry and Physics, 16, 10441-10454, 10.5194/acp-16-10441-2016, 2016.

Tao, J. C., Zhao, C. S., Ma, N., and Liu, P. F.: The impact of aerosol hygroscopic growth on the single-scattering albedo and its application on the NO2 photolysis rate coefficient, Atmos. Chem. Phys., 14, 12055-12067, 10.5194/acp-14-12055-2014, 2014.

Wex, H., Neususs, C., Wendisch, M., Stratmann, F., Koziar, C., Keil, A., Wiedensohler, A., and Ebert, M.: Particle scattering, backscattering, and absorption coefficients: An in situ closure and sensitivity study, J Geophys Res-Atmos, 107, 10.1029/2000jd000234, 2002.

Zhao, G., Zhao, C., Kuang, Y., Tao, J., Tan, W., Bian, Y., Li, J., and Li, C.: Impact of aerosol hygroscopic growth on retrieving aerosol extinction coefficient profiles from elastic-backscatter lidar signals, Atmos. Chem. Phys. Discuss., 2017, 1-24, 10.5194/acp-2017-240, 2017.

Role of black carbons mass size distribution in the direct aerosol radiative forcing

Gang Zhao[1], Jiangchuan Tao[2], Ye Kuang[2], Chuanyang Shen[1], Yingli Yu[1], Chunsheng Zhao[1*]

[1]Department of Atmospheric and Oceanic Sciences, School of Physics, Peking University, Beijing, China

[2]Institute for Environmental and Climate Research, Jinan University, Guangzhou 511443, China

[*]***Correspondence to: Chunsheng Zhao (zcs@pku.edu.cn)***

Abstract

Large uncertainties exist when estimating radiative effects of ambient black carbon (BC) aerosol. Previous studies about the BC aerosol radiative forcing mainly focus on the BC aerosols' mass concentrations and mixing states, while the effects of BC mass size distribution (BCMSD) were not well considered. In this paper, we developed a method by measuring the BCMSD by using a differential mobility analyzer in tandem with an aethalometer. A comprehensive method of multiple charging corrections was proposed and implemented in measuring the BCMSD. Good agreement was obtained between the BC mass concentration integrated from this system and that measured in bulk phase, demonstrating the reliability of our proposed method. Characteristics of the BCMSD and corresponding radiative effects were studied based on field measurements conducted in the North China Plain by using our own designed measurement system. Results showed that the BCMSD had two modes and the mean peak diameters of the two modes were 150 nm and 503 nm respectively. The BCMSD of coarser mode varied significantly under different pollution conditions with peak diameter varying between 430 nm and 580 nm, which gave rise to significant variation in aerosol buck optical properties. The aerosol direct aerosol radiative forcing was estimated to vary by 8.45% for different measured BCMSDs of coarser mode, which shared the same magnitude to the variation associated with assuming different aerosol mixing states (10.5%). Our study reveals that the BCMSD matters as well as their mixing state in estimating the direct aerosol radiative forcing. Knowledge of the BCMSD should be fully considered in climate models.

1 Introduction

Atmospheric black carbon (BC) is the second strongest absorbing components in atmosphere (Bond et al., 2013) but the magnitudes of the warming effects are poorly quantified. When emitted to the surrounding, BC particles transform the morphology from fractal to spherical and then grow as fully compact particles with other components depositing on the BC aerosol (Peng et al., 2016). The variation in the shapes of BC aerosols, together with the variation in the mixing states, can lead to substantial change of aerosol optical properties (Liu et al., 2017;China et al., 2013;Wu et al., 2016a;Wu et al., 2018). BC aerosols also have significant influence on the climate by interacting with clouds (Koch and Del Genio, 2010;Roberts et al., 2008;Stevens and Feingold, 2009), ice and snow (Bond et al., 2013). Recent study shows that the solar absorption of BC can suppress the turbulence in the atmospheric boundary layer (Wilcox et al., 2016). It is found that BC emissions may be responsible for the incensement of droughts and floods in China and India (Menon et al., 2002). In addition, BC can pose a serve threat to human health through inhalation (Nichols et al., 2013;Janssen et al., 2011).

Comprehensive studies have been carried out to evaluate the climate effect of BC based on the measurement of BC mass concentrations (m_{BC}) (Koch et al., 2009;Ramanathan and Carmichael, 2008). The m_{BC} near the ground have been well characterized (Ramachandran and Rajesh, 2007;Ran et al., 2016b;Reddington et al., 2013;Song et al., 2013), and the BC vertical distributions are widely measured and evaluated as well (Ran et al., 2016a;Babu et al., 2011;Ferrero et al., 2011). Despite these measurements, more insights into the BC microphysical properties can help to estimate the influence of BC aerosols on visibility (Zhang et al., 2008), climate (Jacobson, 2001) and human health (Lippmann and Albert, 1969). These microphysical properties include BC morphology (Zhang et al., 2016), density (Zhang et al., 2016), complex refractive index (Bond et al., 2013), hygroscopicity (Zhang et al., 2008;Peng et al., 2017), mixing states (Moffet et al., 2016;Raatikainen et al., 2017), and particularly, the mass size distribution (BCMSD) (Cheng et al., 2012;Cheng and Yang, 2016;Gong et al., 2016). Knowledge of BCMSD is not only helpful to study the mixing state of BC aerosols (Raatikainen et al., 2017), but also essential to model the role of BC in evaluating regional and global climate accurately. BC radiative effects is highly sensitive to the emitted BC particle size distribution (Matsui et al., 2018). The health impacts of BC are significantly related to BCMSD (Turner et al., 2015). Furthermore, the information of BCMSD can help to study the source, the evolution and the mixing state of ambient BC aerosols (Yu et al., 2010).

Many methods have been proposed to measure the BCMSD. For instance, the BCMSD was measured by sampling the aerosol in the size range from about 50 nm to several micrometers onto quartz fiber filter substrates using a micro-orifice uniform deposit impactor (MOUDI) (Venkataraman and Friedlander, 1994;Guo, 2016). Cheng et al. (2014) developed a method to measure the BCMSD by employing two aethalometers in parallel, with one to measure total m_{BC} and the other to measure m_{BC} below specific particle sizes using a size cut-off inlet. The above two methods measure the BCMSD corresponding to the aerodynamic diameter. The Single Particle Soot Photometer (SP2) is developed and widely used because it provides sing particle information, hence the BCMSD and the mixing state of the atmospheric aerosols can be derived directly (Schwarz et al., 2006;Gao et al., 2007;Huang et al., 2012;Singh et al., 2016). The BCMSD corresponding to the ambient aerosol mobility diameter can be measured by using a differential mobility analyzer (DMA) in tandem with SP2 (Raatikainen et al., 2017). However, the laser-induced incandescence method cannot provide reliable information about the particles beyond the range of 70 nm and 400 nm (Moteki and Kondo, 2010), which results in the lack of the knowledge of the BCMSD characteristics for these aerosols over 400 nm. The results from MOUDI find that a great amount of BC locates at the aerodynamic diameter range of between 370 and 1000 nm (Hu et al., 2012;Huang and Yu, 2008). However, the measurements of MOUDI cannot give detailed information of the BCMSD evolution due to the low temporal and diameter resolution (Hu et al., 2012;Huang and Yu, 2008). The characteristics of the BCMSD larger than 370 nm is not well studied due to the limitation of the instrument.

Recently, Ning et al. (2013) and Stabile et al. (2012) proposed a new method to measure the BCMSD by using differential mobility analyzer (DMA) in tandem with Aethalometer (AE). This method has the potential of measuring the BCMSD from 20 nm to 584 nm with high time resolution. We develop and validate the BCMSD measurement system based on the works of Ning et al. (2013). The developed measurement system was employed in a field campaign in the North China Plain. The characteristics of the measured BCMSD were studied based on the field measurement. Furthermore, the effects of BCMSD variations on the aerosol optical properties and corresponding direct aerosol radiative properties were evaluated. The aerosol optical properties were calculated by using the Mie scattering theory. The direct aerosol radiative forcing (DARF) were estimated by using the Santa Barbara DISORT (discrete ordinates radiative transfer) Atmospheric Radiative Transfer (SBDART) model.

The structure of this paper are organized as follows. Section 2 gives the information about the instrument setup and field measurement. Section 3 gives the detailed method used in this study, which contains: 1, conducting multiple charging corrections when deriving the aerosol BCMSD and

2, evaluating the aerosol optical and radiative properties for different BCMSD. Results and discussions are shown in section 4. The conclusion is drawn in the last part.

2 Instrument Setup

The measurement system setup was based on the works of Stabile et al. (2012) and Ning et al. (2013) as schematically shown in Fig.1. The ambient sample aerosol particles were firstly dried to below relative humidity of 30% through a Nafion drying tube before passing through to the DMA (Model 3081, TSI, USA). The DMA scanned aerosol particles with diameter ranges from 12.3 to 697 nm over a period of 285 seconds and started another scanning after a pause of 15 seconds, so one complete cycle took 5 minutes. The sheath and sample flow rates of the DMA were 3 lpm and 0.5 lpm, respectively. The quasi-monodisperse aerosols that passed through the DMA were further divided into two flows: with one lead to an aethalometer (AE51, Model 51, MicroAeth, USA) with a flow rate of 0.2 lpm to measure the absorption coefficient (σ_{abs}) at 1 second time resolution; and the other one with flow rate of 0.3 lpm flow directed to a CPC (Model 3772, TSI, USA), which counted particle number concentrations at 0.1 second resolution. Clean air with a flow rate of 0.7 lpm was used to compensate for the CPC inlet flow, which had default flow rate of 1 lpm. Overall, the combination system of DMA, CPC and AE51 could provide one PNSD and size-resolved σ_{abs} scan every 5 minutes. If the mass absorption coefficient (MAC) at a given diameter is known, the BCMSD can be derived correspondingly.

An aethalometer (AE33, Model 33, Magee, USA) was used to measure the σ_{abs} or $\mathrm{m_{BC}}$ with a time resolution of 1 minute. The mass concentration of particles with diameter smaller than 2.5 μm (PM2.5) was concurrently measured with time resolution of 1 minute during the filed observations by the Tapered Element Oscillating Microbalance (TEOM) Dichotomous Ambient Particulate Monitor (1405-DF), which was an indicator of the pollution conditions.

From 21 March to 9 April in 2017, an intensive field measurement was conducted to characterize of the ambient dry aerosol BCMSD corresponding to aerosol mobility diameter at the AERONET BEIJING_PKU station (N39°59′, E116°18′). This station was located on one roof of Peking University campus in the north west of Beijing, China. There were two main streets, Chengfu Road to the south and Zhongguancun Street to the west that surrounding the station. The aerosol sampled at this station were mainly composed of urban roadside aerosols (Zhao et al., 2018).

3 Methodologies

3.1 Retrieving the BCMSD

Five steps were involved to calculate the BCMSD using the raw data from the measurement system: 1), correcting the ‘loading effect’ and ‘multiple scattering effect’ of σ_{abs} measured by AE51; 2), matching the instrument time between the AE51 and CPC; 3), matching the measured $\sigma_{abs}$and diameter to get the raw size-resolve σ_{abs} that is not involved in multiple charging corrections; 4), conducting the multiple charging corrections of the measured raw size-resolved σ_{abs}; 5), transforming the size-resolved σ_{abs} into BCMSD.

3.1.1 Obtaining the raw size-resolved σ_{abs}

The aethalometer (AE51 and AE33) is a well-developed and widely used instrument to measure the σ_{abs} (Drinovec et al., 2015;Hansen et al., 1984). When absorbing aerosols accumulates on the sample filter of the aethalometer continuously, the σ_{abs} can be determined by concurrently measuring the light intensities I after the fiber filter and the light intensities I_0 transmitted through reference spot which is free of aerosol loading. The light attenuation (ATN) is defined as:

$$\mathrm{ATN} = 100 \cdot \ln(\frac{I_0}{I}). \qquad (1)$$

The total σ_{abs} of the loaded particle on the filter is given by:

$$\sigma_{abs,tot} = \frac{\mathrm{A \cdot ATN}}{100}, \qquad (2)$$

where A is the sample spot area on the filter. The instantaneous σ_{abs} can be calculated through the increment of $\sigma_{abs,tot}$:

$$\sigma_{abs} = \frac{\sigma_{abs,tot}}{\Delta t} = \frac{A \cdot \Delta ATN}{100 \cdot F \cdot \Delta t}, \qquad (3)$$

where F is the flow rate and ΔATN is the ATN variation during the time period of Δt. The $\sigma_{abs,tot}$ can be transformed to m_{BC} when the mass attenuation cross-section (MAC) of BC is known. Traditionally, a constant MAC at 7.7 g/m^2 was used to deduce the m_{BC} (Drinovec et al., 2015).

Corrections of the measured σ_{abs} are necessary because the systematic bias exists due to the prevailingly known ‘loading effect’ and multiple scattering effect (Drinovec et al., 2015;Virkkula et al., 2015;Virkkula et al., 2007). The AE33 can directly provide the corrected σ_{abs} values through measuring two light intensities of two spots with different BC load efficiencies (Drinovec et al., 2015). For AE51, The correcting method in Virkkula et al. (2007) was adopted:

$$\sigma_{abs,\ corrected} = (1 + \mathrm{k} \times ATN)\sigma_{abs,uncorrected}, \qquad (4)$$

where k is the correction factor and a constant value of 0.004 is employed in this study to correct the σ_{abs} from AE51. In the first part of the supplementary material, we showed that the loading effects corrections of $\sigma_{abs}$from AE51 were essential and the value of $\sigma_{abs}$from AE33 could be used as a reference for the measured BCMSD. As for the multiple scattering corrections, Zhang et al. (2018) compared the measured σ_{abs} measured by AE33 and by Multi-Angle Absorption Photometer (MAAP) at Tsinghua University, which is about 2 km away from our measurement site. They recommended a compensation factor of 2.6 to be used and we adopted the same factor in our study.

Time correction was needed because time gaps between voltages implied on the DMA (particle size) and sample particles measured by different instruments were not the same. The time correction procedures were conducted every day during the field measurement to ensure that the time deviations of the CPC and the AE51 were constrained within 2 seconds.

Fig. S3 gave the time series diagram of scanned aerosol diameters by DMA, measured σ_{abs} from AE51, and the aerosol number concentrations counted by CPC. The aerosol PNSD (or size-resolved σ_{abs}) could be calculated by matching the DMA diameter and the measured aerosol number concentrations (or measured $\sigma_{abs}$by simply using the single particle charge ratio for each electrical mobility diameter. These measured PNSD and size-resolved σ_{abs} did not consider the effect of multiple-charging corrections and are labeled as raw aerosol PNSD and raw aerosol size-resolved σ_{abs}.

3.1.2 Multiple charging corrections of raw size-resolved σ_{abs}

In the work of Ning et al. (2013) study, lots of efforts were made to evaluate the performance of the instrument. They considered the diffusion corrections and particle charging corrections. However, the particle charging corrections were limited to single particle charge ratio as they mentioned that they simplified the particle charge correction by applying the peak electrical mobility for the calculation of representative particle size for each mobility bin and single particle charge ratio for each primary mobility. They ignored the fact that the aerosol samples selected by the DMA were quasi-monodisperse with different charges and different diameters.

We proposed a new algorithm for the multi-charge corrections of the size-resolved σ_{abs}. Multi-charge corrections to the measured size distribution were prevailing when the DMA was used to scan the aerosol sizes. When the DMA and CPC are used together to measure the aerosol particle number size distribution (PNSD), the multi-charging corrected aerosol PNSD can be significantly different from the raw measured one (Bau et al., 2014;He and Dhaniyala, 2013;He et al., 2015). As shown in the results part of this study, the multi-charge corrections of the size-resolved σ_{abs} could cause differences in both the magnitude and shape of the size-resolved σ_{abs}. Therefore, it is necessary to perform multi-charge corrections on the size-resolved σ_{abs}. This study developed a new algorithm to correct the size-resolved $\sigma_{abs}$from measured value based on the work of Hagen and Alofs (2007) and Deng et al. (2011).

When the DMA is charged with a negative voltage, those aerosols with a small range of electrical mobility (Z_P) can pass through the DMA:

$$Z_P = \frac{q_{sh}}{2\pi VL}\ln(\frac{r_1}{r_2}), \qquad (5)$$

where q_{sh} is the sheath air flow rate; V is the average voltage on the inner center rod; r_1 and r_2 are the outer and inner radius of annular space respectively. The Z_P is related with D_p by elementary charge (e), number of elementary charges on the particle (n), and gas viscosity poise (μ) with:

$$Z_p = \frac{neC(D_p)}{3\pi\mu D_p}, \qquad (6)$$

where $C(D_p)$ is Cunningham slip correction:

$$\mathrm{C} = 1 + \frac{2\tau}{D_p}(1.142 + 0.558e^{-\frac{0.999D_p}{2\tau}}), \qquad (7)$$

where τ is the gas mean free path. From equation 7, aerosol particles can have the same Z_P despite that they have different n and D_p. At the same time, there exists a relatively larger portion of multiple charged particles for those particles with diameters between 100 nm and 400 nm when the ambient aerosols pass through the X-ray (Tigges et al., 2015;Wiedensohler and Fissan, 1988). Through the above discussion, the selected aerosols by DMA at a given electrical mobility can have different charges which will correspond to different diameters.

When the scan diameter is set as Dp_i for the singly charged particles and the respective voltage of DMA is V_i (i =1, 2, …, I), aerosol particles with electro-mobility of $Z_{p,i}$ (i=1, 2, …, I) can pass through the DMA and the observed σ_{abs} by AE51 can be expressed as:

$$R_i = \int_0^{\infty} G(i,x)A(x)n(x)dx, \qquad (8)$$

where x is the scale parameter, with the definition of $\mathrm{x = log(Dp}_i)$, A(x) is the averageσ_{abs} of single particle for scale parameter x, and $\mathrm{n(x) = dN/dlogDp}$ is aerosol PNSD that is the multiple charging corrected results from the measured aerosol PNSD. We define the kernel function G (i, x), which is crucial to the algorithm, as:

$$\mathrm{G(i,x)} = \sum_{v=1}^{\infty} \emptyset(x,v)\Omega(x,v,i), \qquad (9)$$

where $\emptyset(x,v)$ is the probability of particles that are charged with v charges at the scale parameter of x (Wiedensohler, 1988). $\Omega(x,v,i)$ is the probability of particles that can pass through the DMA with v charges at the scale parameter x (Knutson and Whitby, 1975). In this study, the maximum value of v is 10.

The multiple charging corrections can be expressed as computing the $A(x_i^*)$, in which x_i^* is the predetermined scale parameter from the DMA. To get the numerical integration results of equation 9, the diameter interval that is 1/50 of the measured diameter is used. Thus, equation 9 can be written as

$$R_i = \int_0^{\infty} G(i,x)A(x)n(x)dx = \Delta x_i \sum_{j=1}^{50} \beta_j G(i,x_{i,j})A(x_{i,j})n(x_{i,j}), \qquad (10)$$

where $\beta = \begin{cases} 0.5, & j = 1, J \\ 1, otherwith \end{cases}$; $x_{i,j}$ is the j^th^ (j=1 ,2 ,…, 50) parameter that locates at the parameter x_i and x_{i+1} and $A(x_{i,j})$ (i=1, 2, …, I; j=1, 2, …, 50), the BC mass ratio at scale parameter $x_{i,j}$, is expressed as the linear interpolation of the values at the measured diameters.

$$A(x_{i,j}) = A(x_i) + P_{\mathrm{i}}(x_{i,j} - x_i), \qquad (11)$$

where P_{i} is the slope of the linear interpolation result of

$$A(x_k^*) = C + P_i \cdot x_k^*. \qquad (12)$$

x_k^* refers to these five diameters that are nearest to the predetermined scale parameter x_i. C is the intercept of the linear interpolation result.

With $H_{i,j} = \beta_j \Delta x_i G(i,x_{i,j})n(x_{i,j})$, equation 11 can be written as

$$R_i = \sum_{j=1}^{J} H_{ij}\left[A(x_i) + P_i(x_{i,j} - x_i)\right] = \sum_{j=1}^{J} H_{ij}A(x_i) + \sum_{j=1}^{J} H_{ij}\, P_i x_{i,j} - \sum_{j=1}^{J} H_{ij}\, P_i x_i$$

$$= \sum_{k=1}^{I}(\sum_{j=1}^{J} H_{ij}\,\delta(\mathrm{i-k}))\mathrm{A}(x_k^*)) + \sum_{k=1}^{I}\left(\sum_{j=1}^{J} H_{ij}\, x_{i,j}\delta(\mathrm{i-k})\right)\mathrm{P}_k - \sum_{k=1}^{I}\delta(\mathrm{i-\ k})))P_k x_k^*$$

$$=\sum_{k=1}^{I} Q_{ik}A(x_k^*) + \sum_{k=1}^{I} T_{ik}P_k - \sum_{k=1}^{I} Q_{ik}P_k x_k^*, \qquad (13)$$

where $\delta(\mathrm{x}) = \begin{cases} 0, x \neq 0 \\ 1, x = 0 \end{cases}$,

$$\mathrm{Q}_{ik} = \sum_{j=1}^{J} H_{ij}\delta(i-k), \qquad (14)$$

and $$\mathrm{T}_{ik} = \sum_{j=1}^{J} H_{ij}x_{i,j}\delta(i-k). \qquad (15)$$

By letting the

$$S_i = R_i - \sum_{k=1}^{I} T_{ik} P_k + \sum_{k=1}^{I} Q_{ik} P_k x_k^*. \tag{16}$$

This equation is then expressed as

$$S_i = \sum_{k=1}^{I} Q_{ik} A(x_k^*), \tag{17}$$

or

$$\mathrm{S} = \mathrm{QA}, \tag{18}$$

where S and A are $\mathrm{I} \times 1$ vectors and Q is an $\mathrm{I} \times \mathrm{I}$ matrix. This matrix can be solved by using the non-negative least square method.

Finally, the A(x) can be determined and the corresponding size-resolved σ_{abs} that is multiple charging corrected can be calculated.

3.1.3 Transform the size-resolved σ_{abs} into BCMSD

MAC of different size range is necessary when transform the size-resolved σ_{abs} into BCMSD. The MAC at different size should be different. When the size-resolved σ_{abs} is converted into BCMSD with a constant MAC, the derived BCMSD would be biased.

The size-resolved MAC was calculated using the Mie scattering model (Bohren and Huffman, 2007). Based on the Mie scattering theory, MAC values vary for different aerosol core diameter and different total diameter. Results from SP2 measurement show that the size distribution of the BC core diameter peaked at around 120 nm in Beijing (Zhang et al., 2017). For each aerosol diameter, the MAC value with core diameter of 120 nm was used to transform the BCASD into the BCMSD. MAC values with core diameter at 120±15 nm were calculated and shown in Fig. 2. From Fig. 2, the MAC varied significantly between 3.6 and 9.2 $\mathrm{m^2/g}$. The constant MAC values 7.7 $\mathrm{m^2/g}$ corresponded to the aerosol diameter of 269 nm. The calculated mean MAC values in Fig. 2 under different diameter were used in this study.

3.1.4 Validation of the multiple charging corrections

An example of the multiple charging corrections of the size-resolved σ_{abs} was shown in Fig. 3. The corrections of aerosol PNSD were based on the work of Hagen and Alofs (2007). As shown in Fig. 2(a), the corrected aerosol PNSD was significantly different from the original uncorrected one. There were about half of the measured particles have multiple elementary charge in the size range between 100 and 200 nm. The raw uncorrected aerosol PNSD had a peak value of 10920 $\mathrm{cm^{-3}}$ at 98 nm while the corrected aerosol PNSD reached its peak value of 8450 $\mathrm{cm^{-3}}$ at 98 nm. The peak positions of the raw aerosol particle mass size distribution (PMSD, dm/dlogDp) peaked at 322 nm with a peak value of 86.3 μg/m^3 and the corrected aerosol PMSD had a peak value of 53 μg/m^3 at 461 nm. The peak position of the aerosol PMSD shifted a lot before and after the multiple charging corrections. The similar case for the size-resolved σ_{abs} was shown in Fig. 2(b). The shape of size-resolved σ_{abs} had changed substantially due to the multiple charging corrections. The measured raw BCMSD had a peak diameter near 320 nm and the magnitude of size-resolved σ_{abs} plateau reached 34.3 Mm^{-1}, which was in accordance with the results of Ning et al. (2013), where the multiple charging corrections were not involved. However, the corrected size-resolved σ_{abs} peaks near 410 nm, with a peak value of about 29.5 Mm^{-1}. According to the result, a small amount of σ_{abs} remained in particles with diameter between 100nm and 200nm. The measured size-resolved σ_{abs} changed a lot when multiple charging corrections were implemented, which highlighted the necessity of implementation of appropriate multiple charging corrections

The σ_{abs} integrated from measured size-resolved σ_{abs} changed after multiple charging corrections. Fig. S4 showed the comparison results of the σ_{abs} measured by AE33 and the σ_{abs}integrated from AE51 measurements. The σ_{abs} integrated from uncorrected and corrected size-resolved σ_{abs} versus σ_{abs} measured by AE33 were shown in Fig.S4(a) and Fig.S4(b), respectively. Before multiple charging corrections, the σ_{abs} from uncorrected size-resolved σ_{abs} increased linearly with the σ_{abs} from AE33, with R^2 equaling 0.87, but it was 2.37 times that of AE33 in average. As a comparison, overall magnitude of σ_{abs} integrated from corrected size-resolved σ_{abs} agreed better with that from AE33 with a slope of 1.2. With the discussion above, multiple charging corrections were essential for size-resolved σ_{abs} and BCMSD measurements.

3.2 Fitting the BCMSD by using two log-normal models

Based on the measurement results, the BCMSD had two modes for most of the conditions. The BCMSD are assumed to be of two log-normal distributions as:

$$m_{fit,Dp} = \sum_{i=1,2} \frac{m_i}{\sqrt{2\pi\log(GSD_i)}} \cdot \exp\left(-\frac{[\log(D_p)-\log(D_{m,i})]^2}{2log^2(GSD_{,i})}\right), \qquad (19)$$

Where D_p is the diameter of the aerosols; m_i is the mass of mode i (i=1,2); GSD_i is the geometric standard deviation at mode i (i=1,2), and $D_{m,i}$ is the geometric mean diameter of the mode i (i=1,2). The GSD_i and $D_{m,i}$ can be determined by using the least square method with the objective function as :

$$\mathrm{J} = \sum_{i=1,n}\left(m_{Dp_i} - m_{fit,Dp_i}(D_{m1}, GSD_1, D_{m2}, GSD_2)\right)^2, \qquad (20)$$

Where m_{Dp_i} is the measured mass distribution at Dp_i, while m_{fit,Dp_i} is the fit mass distribution at Dp_i.

3.3 Estimating aerosol optical properties with different BCMSD

The Mie scattering model was used to study the influence of the BCMSD variation on the aerosol optical properties. When running the Mie model, aerosol PNSD and BC were necessary. In this study, The BCMSD was assumed to be log-normal distributed. D_m of the BCMSD was set to vary from 100 nm to 600 nm. Geometric standard deviation (GSD) of the BCMSD was set to be in the range between 1.3 and 1.8. BC was treated as partially externally mixed and the remaining aerosols was treated as core-shell mixed. The ratio of externally mixed $\mathrm{m_{BC}}$ to core-shell $\mathrm{m_{BC}}$ was determined by the method introduced in Ma et al. (2012) and a mean ratio of 0.51 was used. The density and refractive index of BC were set as 1.5 g/cm3 and 1.8+0.54i (Kuang et al., 2015), respectively. The complex refractive index of non-absorbing aerosols was 1.53+10-7i (Wex et al., 2002) at the wavelength of 525 nm. More details of calculating the aerosol optical properties by using the aerosol PNSD and BCMSD, can refer to Kuang et al. (2016).

The aerosol PNSD and m_{BC} used here is the mean result of aerosol PNSD and $\mathrm{m_{BC}}$ over the whole field measurement respectively. The amount of BC particle adopted in this study is the mean value of the $\mathrm{m_{BC}}$ measured by AE33. For each BCMSD, extinction coefficient (σ_{ext}), the scattering coefficient (σ_{sca}), the single scattering albedo (SSA), and the asymmetry factor (g) could be obtained from the output of Mie scattering model.

3.4 Evaluating the DARF with different BCMSD

In this study, the SBDART model (Ricchiazzi et al., 1998) was employed to estimate the DARF. In our study, the instantaneous DARF for cloud free conditions at the top of atmosphere was calculated for irradiance wavelength range from 0.25 to 4 μm. Input of the model required the profiles of aerosol σ_{ext}, SSA, g. These profiles were calculated from the parameterization of the aerosol vertical distributions. Details of calculating the σ_{ext}, SSA and g profiles can refer to part 4 in the supplementary material. In brief, the aerosol σ_{ext}, SSA and g profiles were calculated based on the given aerosol PNSD and BCMSD. The DARF can be estimated using the above aerosol optical profiles.

The aerosol optical properties and the corresponding aerosol optical profiles vary with different BCMSD. Then the DARF should be different for different BCMSD. By estimating the DARF using different aerosol BCMSD, the influence of BCMSD on the aerosol radiative properties can be studied.

4 Results and Discussions

4.1 Measurement results of the BCMSD

The time series of measured PM2.5, aerosol PNSD and BCMSD were shown in Fig. 3. During the observation period, the PM2.5 varied from 0.06 to 220 μg/m^3, with a mean value of 71.5 ± 52.56 μg/m^3. Three periods of heavy PM2.5 loading were observed: (1) PM2.5 increased from around 100 μg/m^3 to 200 μg/m^3 and decreased slowly to 1 μg/m^3 in the period 21-26, March; (2) the PM2.5 accumulated slowly from 28 to 30, March and dissipated quickly from 30, March to 1, April; (3) the rapid accumulation and dissipation of PM2.5 happened during 2 to 5, April. During the last five days, PM2.5 fluctuated between 20 and 120 μg/m^3. For each pollution condition, both the aerosol total number concentrations and the aerosol median diameter increased. The aerosol median diameter varied between 31 nm and 169 nm with a mean value of 78 ± 31 nm.

Our measurements shew that the BCMSD had two modes with the coarser mode ranging between 430 nm and 580 nm in mobility diameter. Many field measurements had revealed that most of the BC mass locates in the aerodynamic diameter range of 320 nm and 560 nm using the MOUDI (Hu et al., 2012;Huang and Yu, 2008). When the aerodynamic diameter was transformed into mobility diameter with assumption a aerosol effective density of 1.3, the measured BC aerodynamic diameter range corresponded to mobility diameter range of 280 nm and 491 nm. Therefore, the measured size range for coarser mode of BCMSD agreed well with the previous measurement.

The measured aerosol in the field site was representative of the urban aerosol. The BC particles emitted by vehicles contributed significantly to the total aerosol BC mass. These BC particles were rarely coated or thinly coated, and the BC core diameter peaked around 120 nm (Zhang et al., 2017). Therefore, the BCMSD of the smaller mode measured in our study corresponded to these uncoated of thinly coated particles.

The total m_{BC} measured by AE33 ranged from 0.1 to 14 μg/m^3 with an average of 5.04 ± 2.64 μg/m^3. Good consistence was achieved between m_{BC} measured by AE33 and m_{BC} calculated from measured BCMSD as shown in Fig. 3(d).

4.2 Evolution of the BCMSD under different polluted conditions

Log-normal distribution was used to fit each mode of the BCMSD by using the least square method as introduced in section 3.2. For each mode, the geometric mean diameter (D_m) and the geometric standard deviation (GSD) of the BCMSD were studied.

During the measurement period, both D_m and GSD of the two modes had changed significantly as shown in Fig S7. The D_m of first and second mode varied from 139 to 161 nm and from 420 to 597 nm, respectively. The corresponding mean D_m was 151 and 520 nm. The D_m of the two modes was found to be positive correlated in Fig. S7(a). When the pollution was released from the beginning to 27, March, the D_m decreased from 597 to 420 nm and from 160 to 140 nm for the coarser mode and the smaller mode respectively. The BC containing aerosols tended to be aged and grew larger when the air surrounding get polluted.

GSD for the coarser mode and the smaller mode showed very different properties as shown in Fig. S7(b). For the second mode, GSD varied from around 1.49 to 1.68 with a mean value of 1.57. The GSD get decreased with the pollution condition, which indicated that BC containing aerosols tend to accumulate to a small range of diameters during the aging processing. This phenomenon was consistent with the fact that larger particles grew relative slower in diameter because the growth ratio of small aerosol particle is proportion to the negative power of it’s diameter. For the first mode, GSD ranged from 1.41 to around 1.86 with a mean value of 1.63. However, GSD of the smaller mode tend to be larger when the surrounding air get cleaner, which might be related to the complex sources of the BC emission. A small amount of fresh emitted BC particles can have substantial influence on the mass size distribution of the smaller mode because the BC concentrations of the smaller mode were small, especially under clean conditions. In general, the GSD of coarser mode was a good indicator of the BC aging process and that of the smaller mode could partially reflect the complex sources of the BC fine particles.

The relationship between the D_m and the GSD for coarser mode was further analyzed by analyzing the distribution of the D_m and GSD. The GSD and D_m had opposite trends as shown in Fig 5. With the increment of the D_m from 420 to 540 nm, the mean value of GSD decreased from around 1.608 to 1.528 while the m_{BC} increased with the D_m. The statistical relationship between D_m and GSD offered a reasonable representation of the BCMSD under different polluted conditions.

In the following work, mean values of the GSD at different D_m were used to for further discussion. The m_{BC} and GSD is positively correlated. The m_{BC} increased from 2.4 to 8.3 μg/m^3 when the D_m increased from 420 to 540 nm.

Note that the GSD get slightly increased with the increment of D_m when D_m was larger than 520 nm. This might be caused by the limit diameter range of BCMSD measuring system which was from 20 to 680 nm. The multiple charge corrections applied to the BCMSD could influence the BCMSD when D_m of the BCMSD was near the end of the scanned diameter and may lead to significant uncertainties to the BCMSD. The measurement results indicated that cases of measured D_m of BCMSD larger than 520 nm were few, demonstrating that this multiple correction effect influenced little on shape of measured BCMSD in most cases.

4.3 Influence of BCMSD variation on the aerosol optical properties

The aerosol optical parameters using the measured mean aerosol PNSD and mean m_{BC} corresponding to different GSD and D_m values were shown in Fig. 6. In Fig. 6(a), the aerosol g varied from 0.603 to 0.627 (variation of 4%). Recent work by Zhao et al, 2017 showed that the aerosol g value in the NCP may vary at a range of 10% due to the change of aerosol PNSD. Aerosol g was more sensitive to D_m when the geometric mean diameter of the BCMSD was lower than 400 nm. However, when the D_m was larger than 400 nm, the g become sensitive to both the D_m and the GSD of BCMSD. Overall, the g varied a little bit (0.02 to 0.609) under the representative conditions during the measurement period. For the aerosol SSA, it was sensitive to the D_m over the whole range as shown in Fig. 6(b). SSA varied between 0.90 and 0.94 under the representative measurement conditions. The σ_{sca} had large changes from 325.6 Mm^{-1} to 364.4 Mm^{-1}. The σ_{sca} was quite sensitive to variations in BCMSD when the D_m was larger than 450 nm as shown in Fig.6c. In addition, variations in σ_{sca} relied more on the variations in D_m when D_m was lower than 400 nm. Within the measurement conditions of BCMSD, the σ_{sca} varied from 328 Mm^{-1} to 345 Mm^{-1}. The measured GSD under different D_m went along with the gradient direction of the σ_{sca}, which mean that the evolution of BCMSD in the atmosphere influenced substantially on σ_{sca}. As for the σ_{abs}, it changed from 24.06 Mm^{-1} to 37.27 Mm^{-1} and the corresponding mass absorption cross section (MAC) was estimated to be in the range of 5.44 to 8.08 m^2/g, suggesting that MAC of the BC aerosols should be carefully studied under different BCMSD conditions.

4.4 Influence of BCMSD on the direct aerosol radiative forcing

The estimated DARF values for different GSD and D_m conditions were estimated. When estimating the DARF, the measured mean aerosol PNSD and mean BC mass concentration were used. The results of estimated DARF were shown in Fig. 7(a). DARF at the surface varied from --4.3 w/m^2 to -3.59 w/m^2 for different BCMSD. Within the measured BCMSD range, the DARF varied from -3.97w/m^2 to -3.67w/m^2, which corresponding to 8.45% of variation. The heating rate within the mixed layer was a powerful indicator of the BC particles' absorbing effects, which may help evaluate the development of the boundary layer. The calculated mean heating rate within the mixed layer changed from 2.16 K/day to 2.65 K/day for different D_m and GSD, as shown in Fig. 7(b). The heating rate with the measured BCMSD range could change from 2.24 to 2.50 with a variation of 11.6%.

Mixing states of BC play significant roles in calculations of aerosol optical properties and estimations of DARF (Jacobson, 2001). As a comparison, we estimated the DARF under different conditions of BC mixing state: (1) internally mixed, (2) externally mixed and (3) core-shell mixed. Table 1 gave the estimated DARF and mean heating rate within the mixed layer under different mixing state conditions. Results showed that the DARF under different BC mixing states conditions may change by 10.50%, which shared the same magnitude with 8.45% variation of DARF caused by BCMSD variations. In addition, the heating rate was estimated to vary by 9.71%. These results highlighted that the BCMSD plays significant roles in variations of aerosol optical properties and estimations of DARF as well as the air heating rate caused by the existence of BC particles. It was recommended that a real time measured BCMSD be used when estimating the aerosol DARF, instead of a constant one. The BCMSD was as important as that of the BC mixing states.

5 Conclusions

Knowledge of the BC microphysical properties especially the size-dependent information can help reduce the uncertainties when estimating the aerosol radiative effects. BCMSD is an important quantity in its own right, being directly and indirectly applicable to determination the sources, aging processes and mixing states of BC aerosols. In this study, the characteristics of BCMSD were studied from the field measurement results by using our own developed measurement algorithm.

The BCMSD measurement system was developed and validated based on the works of Ning et al. (2013) by using differential mobility analyzer (DMA) in tandem with Aethalometer (AE). When deriving the BCMSD, a comprehensive multiple charging correction algorithm was proposed and implied. This algorithm was validated by closure study between the measured total m_{BC} from AE33 and the m_{BC} integrated from the measured BCMSD using the datasets from field measurements. Results showed that the multiple charging corrections could significantly change the shapes and magnitudes of the raw measured BCMSD. The accurate BCMSD characteristics could be obtained by our proposed method in this paper.

The developed measurement system was employed in a field campaign in the North China Plain from 21 Match to 9 April in 2017. The BCMSD was found to have two quasi-lognormal modes with peaks at around 150 nm and 500 nm, respectively. These two modes were consistent with the previous measurement results by MOUDI (Wang et al., 2015;Hu et al., 2012). The amount of the BC mass concentrations for the coarser mode peaks were about twice to that of the smaller mode.

The characteristic of the BCMSD was studied by fitting the shape of BCMSD with a bi-normal distribution. The relationships between the fitted D_m and GSD were statistically studied. During the aging processing, the opposite trends for the D_m and GSD were found for coarser mode. This is the first time that the coarser mode of the BCMSD were synthetically studied. The BCMSD of coarser mode varied significantly under different pollution conditions with peak diameter changed between 430 and 580 nm. However, the relationship between the D_m and GSD for smaller mode BC aerosols were more complex due to the complex sources.

When the BCMSD were changed with the polluted condition, the corresponding aerosol optical properties changes significantly. Sensitivity studies found that the aerosol g varies from 0.603 to 0.627 due to the variations in BCMSD. Aerosol g was more sensitive to D_m when the geometric mean diameter of the BCMSD is in the range of 300 nm and 370 nm. The SSA can changed from 0.90 to 0.94. The σ_{sca} experienced significant change with the variation of BCMSD from 325.6 Mm^{-1} to 364.4 Mm^{-1} and the σ_{abs} changed in the range between 24.064 Mm^{-1} and 37.27 Mm^{-1}. The corresponding BC MAC was calculated to be in the range between 5.44 and 8.08 m^2/g.

The variations in DARF were estimated due to the variations of the BCMSD by using the SBDART model. Results showed that the DARF can varies by about 8.45% for different BCMSD and the heating rate for different measured BCMSD conditions could change from 2.24 to 2.50, corresponding to a variation of 11.6%. At the same time, the variations in DARF due to the variations in the BC mixing state was estimated to be 10.5% and that of the heating rate is 8.45%. Thus, the variations of the BCMSD may had significant influence on the aerosol radiative budget and an accurate measurement of BCMSD was very necessary.

Competing interests. The authors declare that they have no conflict of interest.

Data availability. The data used in this study is available when requesting the authors.

Author contributions. GZ, CZ, JT and YK designed and conducted the experiments; CS, YY, CZ and GZ discussed the results.

Acknowledgments. This work is supported by the National Key R&D Program of China (2016YFA0602001) and the National Natural Science Foundation of China (41590872).

References

Babu, S. S., Sreekanth, V., Moorthy, K. K., Mohan, M., Kirankumar, N. V. P., Subrahamanyam, D. B., Gogoi, M. M., Kompalli, S. K., Beegum, N., Chaubey, J. P., Kumar, V. H. A., and Manchandab, R. K.: Vertical profiles of aerosol black carbon in the atmospheric boundary layer over a tropical coastal station: Perturbations during an annular solar eclipse, Atmospheric Research, 99, 471-478, 10.1016/j.atmosres.2010.11.019, 2011.

Bau, S., Bemer, D., Grippari, F., Appert-Collin, J.-C., and Thomas, D.: Determining the effective density of airborne nanoparticles using multiple charging correction in a tandem DMA/ELPI setup, Journal of Nanoparticle Research, 16, 10.1007/s11051-014-2629-2, 2014.

Bohren, C. F., and Huffman, D. R.: Absorption and Scattering by a Sphere, in: Absorption and Scattering of Light by Small Particles, Wiley-VCH Verlag GmbH, 82-129, 2007.

Bond, T. C., Doherty, S. J., Fahey, D. W., Forster, P. M., Berntsen, T., DeAngelo, B. J., Flanner, M. G., Ghan, S., Karcher, B., Koch, D., Kinne, S., Kondo, Y., Quinn, P. K., Sarofim, M. C., Schultz, M. G., Schulz, M., Venkataraman, C., Zhang, H., Zhang, S., Bellouin, N., Guttikunda, S. K., Hopke, P. K., Jacobson, M. Z., Kaiser, J. W., Klimont, Z., Lohmann, U., Schwarz, J. P., Shindell, D., Storelvmo, T., Warren, S. G., and Zender, C. S.: Bounding the role of black carbon in the climate system: A scientific assessment, J Geophys Res-Atmos, 118, 5380-5552, 10.1002/jgrd.50171, 2013.

Cheng, Y. F., Su, H., Rose, D., Gunthe, S. S., Berghof, M., Wehner, B., Achtert, P., Nowak, A., Takegawa, N., Kondo, Y., Shiraiwa, M., Gong, Y. G., Shao, M., Hu, M., Zhu, T., Zhang, Y. H., Carmichael, G. R., Wiedensohler, A., Andreae, M. O., and Pöschl, U.: Size-resolved measurement of the mixing state of soot in the megacity Beijing, China: diurnal cycle, aging and parameterization, Atmospheric Chemistry and Physics, 12, 4477-4491, 10.5194/acp-12-4477-2012, 2012.

Cheng, Y. H., Liao, C. W., Liu, Z. S., Tsai, C. J., and Hsi, H. C.: A size-segregation method for monitoring the diurnal characteristics of atmospheric black carbon size distribution at urban traffic sites, Atmospheric Environment, 90, 78-86, 2014.

Cheng, Y. H., and Yang, L. S.: Characteristics of Ambient Black Carbon Mass and Size-Resolved Particle Number Concentrations during Corn Straw Open-Field Burning Episode Observations at a Rural Site in Southern Taiwan, Int J Environ Res Public Health, 13, 10.3390/ijerph13070688, 2016.

China, S., Mazzoleni, C., Gorkowski, K., Aiken, A. C., and Dubey, M. K.: Morphology and mixing state of individual freshly emitted wildfire carbonaceous particles, Nature communications, 4, 2122, 2013.

Deng, Z. Z., Zhao, C. S., Ma, N., Liu, P. F., Ran, L., Xu, W. Y., Chen, J., Liang, Z., Liang, S., Huang, M. Y., Ma, X. C., Zhang, Q., Quan, J. N., Yan, P., Henning, S., Mildenberger, K., Sommerhage, E., Schafer, M., Stratmann, F., and Wiedensohler, A.: Size-resolved and bulk activation properties of aerosols in the North China Plain, Atmospheric Chemistry and Physics, 11, 3835-3846, 10.5194/acp-11-3835-2011, 2011.

Drinovec, L., Močnik, G., Zotter, P., Prévôt, A. S. H., Ruckstuhl, C., Coz, E., Rupakheti, M., Sciare, J., Müller, T., Wiedensohler, A., and Hansen, A. D. A.: The "dual-spot" Aethalometer: an improved measurement of aerosol black carbon with real-time loading compensation, Atmospheric Measurement Techniques, 8, 1965-1979, 10.5194/amt-8-1965-2015, 2015.

Ferrero, L., Mocnik, G., Ferrini, B. S., Perrone, M. G., Sangiorgi, G., and Bolzacchini, E.: Vertical profiles of aerosol absorption coefficient from micro-Aethalometer data and Mie calculation over Milan, Science of the Total Environment, 409, 2824-2837, 10.1016/j.scitotenv.2011.04.022, 2011.

Gao, R. S., Schwarz, J. P., Kelly, K. K., Fahey, D. W., Watts, L. A., Thompson, T. L., Spackman, J. R., Slowik, J. G., Cross, E. S., Han, J. H., Davidovits, P., Onasch, T. B., and Worsnop, D. R.: A Novel Method for Estimating Light-Scattering Properties of Soot Aerosols Using a Modified Single-Particle Soot Photometer, Aerosol Sci. Technol., 41, 125-135, 10.1080/02786820601118398, 2007.

Gong, X., Zhang, C., Chen, H., Nizkorodov, S. A., Chen, J., and Yang, X.: Size distribution and mixing state of black carbon particles during a heavy air pollution episode in Shanghai, Atmos. Chem. Phys., 16, 5399-5411, 10.5194/acp-16-5399-2016, 2016.

Guo, Y.: Characteristics of size-segregated carbonaceous aerosols in the Beijing-Tianjin-Hebei region, Environ. Sci. Pollut. Res., 23, 13918-13930, 10.1007/s11356-016-6538-z, 2016.

Hagen, D. E., and Alofs, D. J.: Linear Inversion Method to Obtain Aerosol Size Distributions from Measurements with a Differential Mobility Analyzer, Aerosol Sci. Technol., 2, 465-475, 10.1080/02786828308958650, 2007.

Hansen, A. D. A., Rosen, H., and Novakov, T.: The aethalometer — An instrument for the real-time measurement of optical absorption by aerosol particles, Science of The Total Environment, 36, 191-196, http://dx.doi.org/10.1016/0048-9697(84)90265-1, 1984.

He, M., and Dhaniyala, S.: A multiple charging correction algorithm for scanning electrical mobility spectrometer data, Journal of Aerosol Science, 61, 13-26, 10.1016/j.jaerosci.2013.03.007, 2013.

He, M., Dhaniyala, S., and Wagner, M.: Aerosol Filtration with Mobility-Classified Particles: Role of Multiply Charged Particles in Skewing Penetration Measurements, Aerosol Sci. Technol., 49, 704-715, 10.1080/02786826.2015.1062467, 2015.

Hu, M., Peng, J., Sun, K., Yue, D., Guo, S., Wiedensohler, A., and Wu, Z.: Estimation of size-resolved ambient particle density based on the measurement of aerosol number, mass, and chemical size distributions in the winter in Beijing, Environ Sci Technol, 46, 9941-9947, 10.1021/es204073t, 2012.

Huang, X.-F., Sun, T.-L., Zeng, L.-W., Yu, G.-H., and Luan, S.-J.: Black carbon aerosol characterization in a coastal city in South China using a single particle soot photometer, Atmospheric Environment, 51, 21-28, 10.1016/j.atmosenv.2012.01.056, 2012.

Huang, X. F., and Yu, J. Z.: Size distributions of elemental carbon in the atmosphere of a coastal urban area in South China: characteristics, evolution processes, and implications for the mixing state, Atmospheric Chemistry and Physics, 8, 5843-5853, 2008.

Jacobson, M. Z.: Strong radiative heating due to the mixing state of black carbon in atmospheric aerosols, Nature, 409, 695-697, 2001.

Janssen, N. A. H., Hoek, G., Simic-Lawson, M., Fischer, P., van Bree, L., ten Brink, H., Keuken, M., Atkinson, R. W., Anderson, H. R., Brunekreef, B., and Cassee, F. R.: Black Carbon as an Additional Indicator of the Adverse Health Effects of Airborne Particles Compared with PM10 and PM2.5, Environ Health Persp, 119, 1691-1699, 10.1289/ehp.1003369, 2011.

KlausWilleke, and Baron, P.: Aerosol measurement : principles, techniques, and applications, Van

Nostrand Reinhold, 807-808 pp., 1996.

Knutson, E. O., and Whitby, K. T.: Aerosol classification by electric mobility: apparatus, theory, and applications, Journal of Aerosol Science, 6, 443-451, 1975.

Koch, D., Schulz, M., Kinne, S., and Mcnaughton, C.: Evaluation of black carbon estimations in global aerosol models, Atmospheric Chemistry & Physics, 9, 9001-9026, 2009.

Koch, D., and Del Genio, A. D.: Black carbon semi-direct effects on cloud cover: review and synthesis, Atmos. Chem. Phys., 10, 7685-7696, 10.5194/acp-10-7685-2010, 2010.

Kuang, Y., Zhao, C. S., Tao, J. C., and Ma, N.: Diurnal variations of aerosol optical properties in the North China Plain and their influences on the estimates of direct aerosol radiative effect, Atmos. Chem. Phys., 15, 5761-5772, 10.5194/acp-15-5761-2015, 2015.

Kuang, Y., Zhao, C. S., Tao, J. C., Bian, Y. X., and Ma, N.: Impact of aerosol hygroscopic growth on the direct aerosol radiative effect in summer on North China Plain, Atmospheric Environment, 147, 224-233, 2016.

Lippmann, M., and Albert, R. E.: The Effect of Particle Size on the Regional Deposition of Inhaled Aerosols in the Human Respiratory Tract, American Industrial Hygiene Association Journal, 30, 257-275, 10.1080/00028896909343120, 1969.

Liu, D., Whitehead, J., Alfarra, M. R., Reyes-Villegas, E., Spracklen, Dominick V., Reddington, Carly L., Kong, S., Williams, Paul I., Ting, Y.-C., Haslett, S., Taylor, Jonathan W., Flynn, Michael J., Morgan, William T., McFiggans, G., Coe, H., and Allan, James D.: Black-carbon absorption enhancement in the atmosphere determined by particle mixing state, Nature Geoscience, 10, 184-188, 10.1038/ngeo2901, 2017.

Ma, N., Zhao, C. S., Müller, T., Cheng, Y. F., Liu, P. F., Deng, Z. Z., Xu, W. Y., Ran, L., Nekat, B., van Pinxteren, D., Gnauk, T., Müller, K., Herrmann, H., Yan, P., Zhou, X. J., and Wiedensohler, A.: A new method to determine the mixing state of light absorbing carbonaceous using the measured aerosol optical properties and number size distributions, Atmos. Chem. Phys., 12, 2381-2397, 10.5194/acp-12-2381-2012, 2012.

Matsui, H., Hamilton, D. S., and Mahowald, N. M.: Black carbon radiative effects highly sensitive to emitted particle size when resolving mixing-state diversity, Nature communications, 9, 3446, 10.1038/s41467-018-05635-1, 2018.

Menon, S., Hansen, J., Nazarenko, L., and Luo, Y.: Climate effects of black carbon aerosols in China and India, Science, 297, 2250-2253, 10.1126/science.1075159, 2002.

Moffet, R. C., amp, apos, Brien, R. E., Alpert, P. A., Kelly, S. T., Pham, D. Q., Gilles, M. K., Knopf, D. A., and Laskin, A.: Morphology and mixing of black carbon particles collected in central California during the CARES field study, Atmospheric Chemistry and Physics, 16, 14515-14525, 10.5194/acp-16-14515-2016, 2016.

Moteki, N., and Kondo, Y.: Dependence of Laser-Induced Incandescence on Physical Properties of Black Carbon Aerosols: Measurements and Theoretical Interpretation, Aerosol Sci. Technol., 44, 663-675, Pii 924375405
10.1080/02786826.2010.484450, 2010.

Nichols, J. L., Owens, E. O., Dutton, S. J., and Luben, T. J.: Systematic review of the effects of black carbon on cardiovascular disease among individuals with pre-existing disease, International Journal of Public Health, 58, 707-724, 2013.

Ning, Z., Chan, K. L., Wong, K. C., Westerdahl, D., Močnik, G., Zhou, J. H., and Cheung, C. S.: Black carbon mass size distributions of diesel exhaust and urban aerosols measured using differential mobility analyzer in tandem with Aethalometer, Atmospheric Environment, 80, 31-40, 10.1016/j.atmosenv.2013.07.037, 2013.

Ohata, S., Moteki, N., and Kondo, Y.: Evaluation of a Method for Measurement of the Concentration and Size Distribution of Black Carbon Particles Suspended in Rainwater, Aerosol Sci. Technol., 45, 1326-1336, 2011.

Peng, J., Hu, M., Guo, S., Du, Z., Zheng, J., Shang, D., Levy Zamora, M., Zeng, L., Shao, M., Wu, Y.-S., Zheng, J., Wang, Y., Glen, C. R., Collins, D. R., Molina, M. J., and Zhang, R.: Markedly enhanced absorption and direct radiative forcing of black carbon under polluted urban environments, Proceedings of the National Academy of Sciences, 201602310, 10.1073/pnas.1602310113, 2016.

Peng, J., Hu, M., Guo, S., Du, Z., Shang, D., Zheng, J., Zheng, J., Zeng, L., Shao, M., Wu, Y., Collins, D., and Zhang, R.: Ageing and hygroscopicity variation of black carbon particles in Beijing measured by a quasi-atmospheric aerosol evolution study (QUALITY) chamber, Atmospheric Chemistry and Physics, 17, 10333-10348, 10.5194/acp-17-10333-2017, 2017.

Raatikainen, T., Brus, D., Hooda, R. K., Hyvärinen, A.-P., Asmi, E., Sharma, V. P., Arola, A., and Lihavainen, H.: Size-selected black carbon mass distributions and mixing state in polluted and clean environments of northern India, Atmospheric Chemistry and Physics, 17, 371-383, 10.5194/acp-17-371-2017, 2017.

Ramachandran, S., and Rajesh, T. A.: Black carbon aerosol mass concentrations over Ahmedabad, an urban location in western India: Comparison with urban sites in Asia, Europe, Canada, and the United States, J Geophys Res-Atmos, 112, Artn D06211
10.1029/2006jd007488, 2007.

Ramanathan, V., and Carmichael, G.: Global and regional climate changes due to black carbon, Nature Geoscience, 1, 221-227, 10.1038/ngeo156, 2008.

Ran, L., Deng, Z., Xu, X., Yan, P., Lin, W., Wang, Y., Tian, P., Wang, P., Pan, W., and Lu, D.: Vertical profiles of black carbon measured by a micro-aethalometer in summer in the North China Plain, Atmospheric Chemistry and Physics, 16, 10441-10454, 10.5194/acp-16-10441-2016, 2016a.

Ran, L., Deng, Z. Z., Wang, P. C., and Xia, X. A.: Black carbon and wavelength-dependent aerosol absorption in the North China Plain based on two-year aethalometer measurements, Atmospheric Environment, 142, 132-144, 10.1016/j.atmosenv.2016.07.014, 2016b.

Reddington, C. L., McMeeking, G., Mann, G. W., Coe, H., Frontoso, M. G., Liu, D., Flynn, M., Spracklen, D. V., and Carslaw, K. S.: The mass and number size distributions of black carbon aerosol over Europe, Atmospheric Chemistry and Physics, 13, 4917-4939, 10.5194/acp-13-4917-2013, 2013.

Ricchiazzi, P., Yang, S., Gautier, C., and Sowle, D.: SBDART: A Research and Teaching Software Tool for Plane-Parallel Radiative Transfer in the Earth's Atmosphere, Bulletin of the American Meteorological Society, 79, 2101-2114, 10.1175/1520-0477(1998)079<2101:sarats>2.0.co;2, 1998.

Roberts, G. C., Ramana, M. V., Corrigan, C., Kim, D., and Ramanathan, V.: Simultaneous observations of aerosol-cloud-albedo interactions with three stacked unmanned aerial vehicles, Proceedings of the National Academy of Sciences of the United States of America, 105, 7370-7375, 10.1073/pnas.0710308105, 2008.

Schwarz, J. P., Gao, R. S., Fahey, D. W., Thomson, D. S., Watts, L. A., Wilson, J. C., Reeves, J. M., Darbeheshti, M., Baumgardner, D. G., Kok, G. L., Chung, S. H., Schulz, M., Hendricks, J., Lauer, A., Kärcher, B., Slowik, J. G., Rosenlof, K. H., Thompson, T. L., Langford, A. O., Loewenstein, M., and Aikin, K. C.: Single-particle measurements of midlatitude black carbon and light-scattering aerosols from the boundary layer to the lower stratosphere, Journal of Geophysical Research, 111, 10.1029/2006jd007076, 2006.

Singh, S., Fiddler, M. N., and Bililign, S.: Measurement of size-dependent single scattering albedo of fresh biomass burning aerosols using the extinction-minus-scattering technique with a combination of cavity ring-down spectroscopy and nephelometry, Atmospheric Chemistry and Physics, 16, 13491-13507, 10.5194/acp-16-13491-2016, 2016.

Song, S., Wu, Y., Xu, J., Ohara, T., Hasegawa, S., Li, J., Yang, L., and Hao, J.: Black carbon at a roadside site in Beijing: Temporal variations and relationships with carbon monoxide and particle number size distribution, Atmospheric Environment, 77, 213-221, https://doi.org/10.1016/j.atmosenv.2013.04.055, 2013.

Stabile, L., Fuoco, F. C., and Buonanno, G.: Characteristics of particles and black carbon emitted by combustion of incenses, candles and anti-mosquito products, Building and Environment, 56, 184-191, 10.1016/j.buildenv.2012.03.005, 2012.

Stevens, B., and Feingold, G.: Untangling aerosol effects on clouds and precipitation in a buffered system, Nature, 461, 607-613, 10.1038/nature08281, 2009.

Tigges, L., Wiedensohler, A., Weinhold, K., Gandhi, J., and Schmid, H. J.: Bipolar charge distribution of a soft X-ray diffusion charger, Journal of Aerosol Science, 90, 77-86, 10.1016/j.jaerosci.2015.07.002, 2015.

Turner, M. D., Henze, D. K., Hakami, A., Zhao, S. L., Resler, J., Carmichael, G. R., Stanier, C. O., Baek, J., Sandu, A., Russell, A. G., Nenes, A., Jeong, G. R., Capps, S. L., Percell, P. B., Pinder, R. W., Napelenok, S. L., Bash, J. O., and Chai, T. F.: Differences Between Magnitudes and Health Impacts of BC Emissions Across the United States Using 12 km Scale Seasonal Source Apportionment, Environmental Science & Technology, 49, 4362-4371, 10.1021/es505968b, 2015.

Venkataraman, C., and Friedlander, S. K.: Size distributions of polycyclic aromatic hydrocarbons and elemental carbon. 2. Ambient measurements and effects of atmospheric processes, Environmental Science & Technology, 28, 563, 1994.

Virkkula, A., Makela, T., Hillamo, R., Yli-Tuomi, T., Hirsikko, A., Hameri, K., and Koponen, I. K.: A simple procedure for correcting loading effects of aethalometer data, J Air Waste Manag Assoc, 57, 1214-1222, 10.3155/1047-3289.57.10.1214, 2007.

Virkkula, A., Chi, X., Ding, A., Shen, Y., Nie, W., Qi, X., Zheng, L., Huang, X., Xie, Y., Wang, J., Petaja, T., and Kulmala, M.: On the interpretation of the loading correction of the aethalometer, Atmospheric Measurement Techniques, 8, 4415-4427, 10.5194/amt-8-4415-2015, 2015.

Wang, Q. Y., Huang, R. J., Cao, J. J., Tie, X. X., Ni, H. Y., Zhou, Y. Q., Han, Y. M., Hu, T. F., Zhu, C. S., Feng, T., Li, N., and Li, J. D.: Black carbon aerosol in winter northeastern Qinghai–Tibetan Plateau, China: the source, mixing state and optical property, Atmospheric Chemistry and Physics, 15, 13059-13069, 10.5194/acp-15-13059-2015, 2015.

Wex, H., Neusüß, C., Wendisch, M., Stratmann, F., Koziar, C., Keil, A., Wiedensohler, A., and Ebert, M.: Particle scattering, backscattering, and absorption coefficients: An in situ closure and sensitivity study, Journal of Geophysical Research: Atmospheres, 107, LAC 4-1-LAC 4-18, 10.1029/2000jd000234, 2002.

Wiedensohler, A.: An approximation of the bipolar charge distribution for particles in the submicron size range, Journal of Aerosol Science, 19, 387-389, 1988.

Wiedensohler, A., and Fissan, H. J.: Aerosol charging in high purity gases, Journal of Aerosol Science, 19, 867-870, 1988.

Wilcox, E. M., Thomas, R. M., Praveen, P. S., Pistone, K., Bender, F. A. M., and Ramanathan, V.: Black carbon solar absorption suppresses turbulence in the atmospheric boundary layer, Proceedings of the National Academy of Sciences, 113, 11794-11799, 10.1073/pnas.1525746113, 2016.

Wu, Y., Cheng, T., Zheng, L., and Chen, H.: Effect of morphology on the optical properties of soot aggregated with spheroidal monomers, Journal of Quantitative Spectroscopy & Radiative Transfer, 168, 158-169, 2016a.

Wu, Y., Wang, X., Tao, J., Huang, R., Tian, P., Cao, J., Zhang, L., Ho, K.-F., and Zhang, R.: Size distribution and source of black carbon aerosol in urban Beijing during winter haze episodes, Atmospheric Chemistry and Physics Discussions, 1-25, 10.5194/acp-2016-1096, 2016b.

Wu, Y., Cheng, T., Liu, D., Allan, J. D., Zheng, L., and Chen, H.: Light Absorption Enhancement of Black Carbon Aerosol Constrained by Particle Morphology, Environ Sci Technol, 52, 6912-6919, 10.1021/acs.est.8b00636, 2018.

Yu, H., and Yu, J. Z.: Modal Characteristics of Elemental and Organic Carbon in an Urban Location in Guangzhou, China, Aerosol Sci. Technol., 43, 1108-1118, 2009.

Yu, H., Wu, C., Wu, D., and Yu, J. Z.: Size distributions of elemental carbon and its contribution to light extinction in urban and rural locations in the pearl river delta region, China, Atmos. Chem. Phys., 10, 5107-5119, 10.5194/acp-10-5107-2010, 2010.

Zhang, R., Khalizov, A. F., Pagels, J., Zhang, D., Xue, H., and McMurry, P. H.: Variability in morphology, hygroscopicity, and optical properties of soot aerosols during atmospheric processing, Proceedings of the National Academy of Sciences of the United States of America, 105, 10291-10296, 10.1073/pnas.0804860105, 2008.

Zhang, Y., Zhang, Q., Cheng, Y., Su, H., Kecorius, S., Wang, Z., Wu, Z., Hu, M., Zhu, T., Wiedensohler, A., and He, K.: Measuring the morphology and density of internally mixed black carbon with SP2 and VTDMA: new insight into the absorption enhancement of black carbon in the atmosphere, Atmospheric Measurement Techniques, 9, 1833-1843, 10.5194/amt-9-1833-2016, 2016.

Zhang, Y., Su, H., Kecorius, S., Wang, Z., Hu, M., Zhu, T., He, K., Wiedensohler, A., Zhang, Q., and Cheng, Y.: Mixing State of Refractory Black Carbon of the North China Plain Regional Aerosol Combining a Single Particle Soot Photometer and a Volatility Tandem Differential Mobility Analyzer, Atmospheric Chemistry and Physics Discussions, 1-27, 10.5194/acp-2017-222, 2017.

Zhang, Y., Zhang, Q., Cheng, Y., Su, H., Li, H., Li, M., Zhang, X., Ding, A., and He, K.: Amplification of light absorption of black carbon associated with air pollution, Atmospheric Chemistry and Physics, 18, 9879-9896, 10.5194/acp-18-9879-2018, 2018.

Zhao, G., Zhao, C., Kuang, Y., Bian, Y., Tao, J., Shen, C., and Yu, Y.: Calculating the aerosol asymmetry factor based on measurements from the humidified nephelometer system, Atmospheric Chemistry and Physics, 18, 9049-9060, 10.5194/acp-18-9049-2018, 2018.

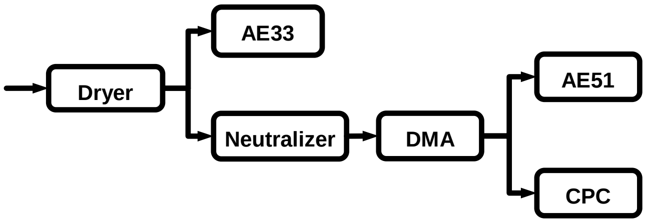

Figure 1. The schematic diagram of the instrument setup.

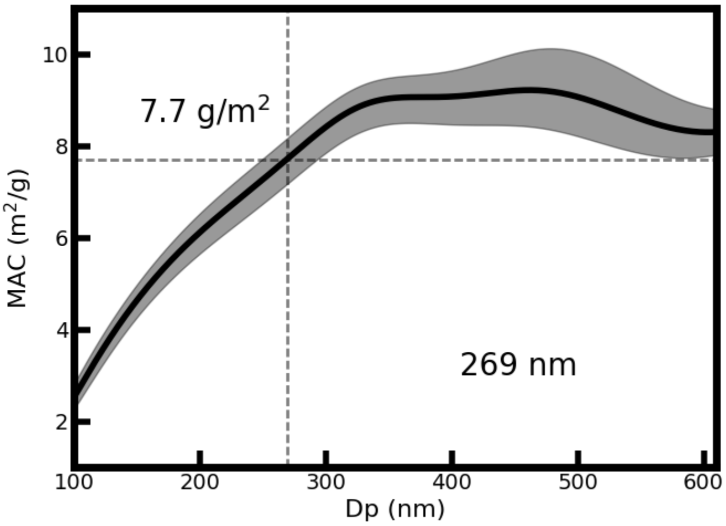

Figure 2. Calculated mass absorption coefficient of different aerosol.

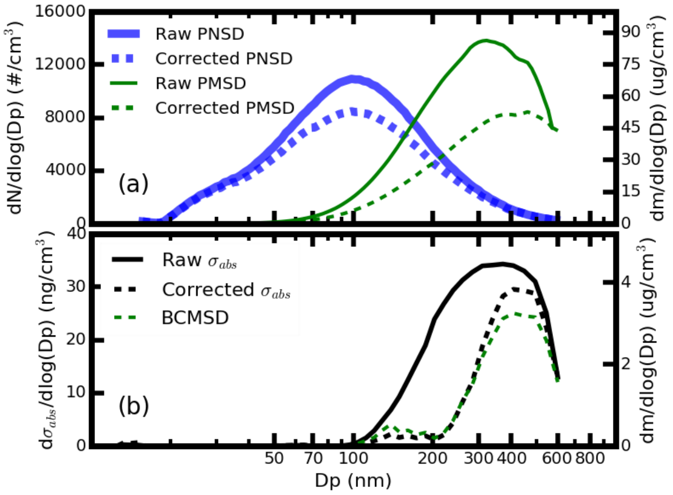

Figure 3. Case of multiple charging correction processing. (a) the multiple charging correction of the aerosol PNSD and aerosol PMSD, (b) the multiple charging correction of the size-resolved σ_{abs}. The solid line is the measured results without multiple charging corrections and the dotted line is the multiple charging corrections results.

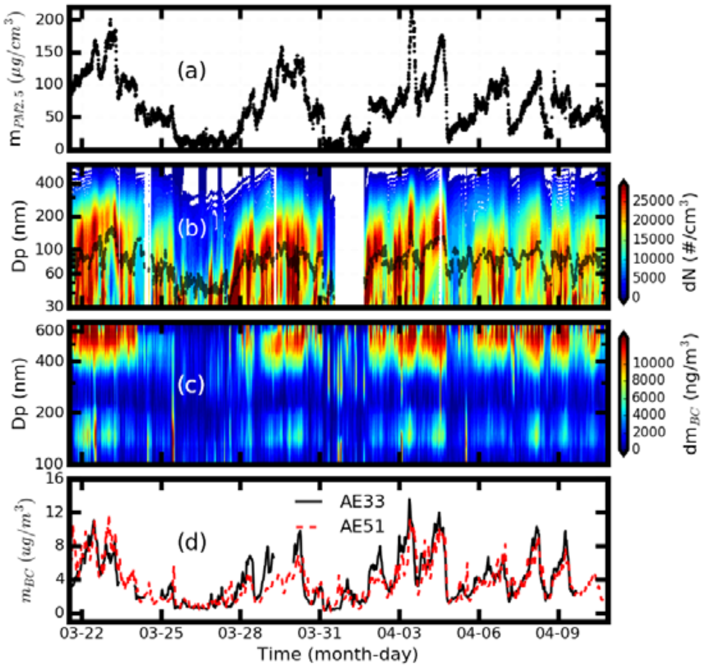

Figure 4. The measured time series of mass concentrations for (a) the PM2.5; (b) the aerosol PNSD in filled color, the geometric median diameter in dotted line;(c) the BCMSD and (d) the m_{BC} by AE33 (black) and m_{BC} from integrated BCMSD from AE51 (red).

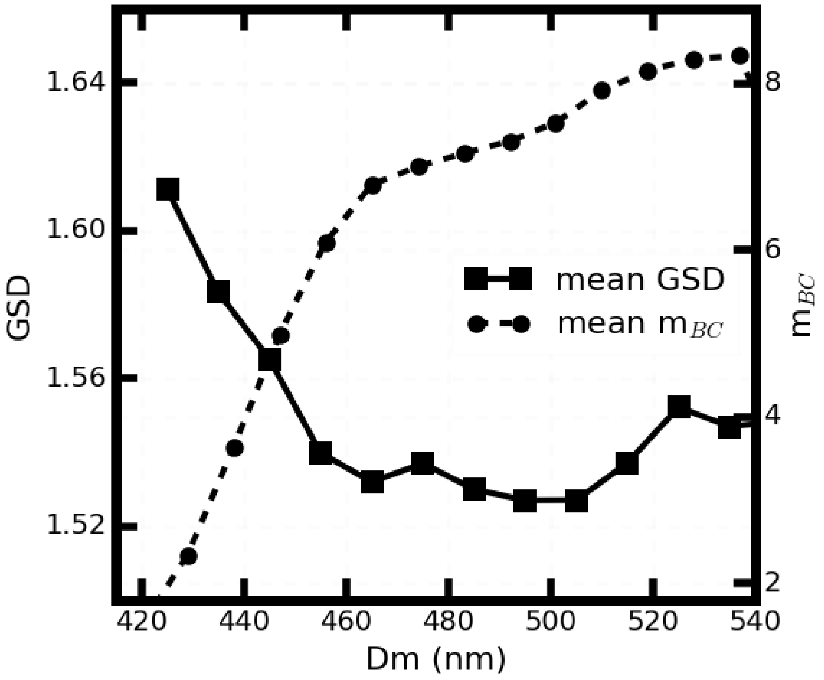

Figure 5. The relationship between the Dm and the GSD. The black dots show the real measured Dm and GSD. The black line shows the mean results of the GSD for different Dm. The black line marked with square shows the variation of mean m_{BC} with the Dm.

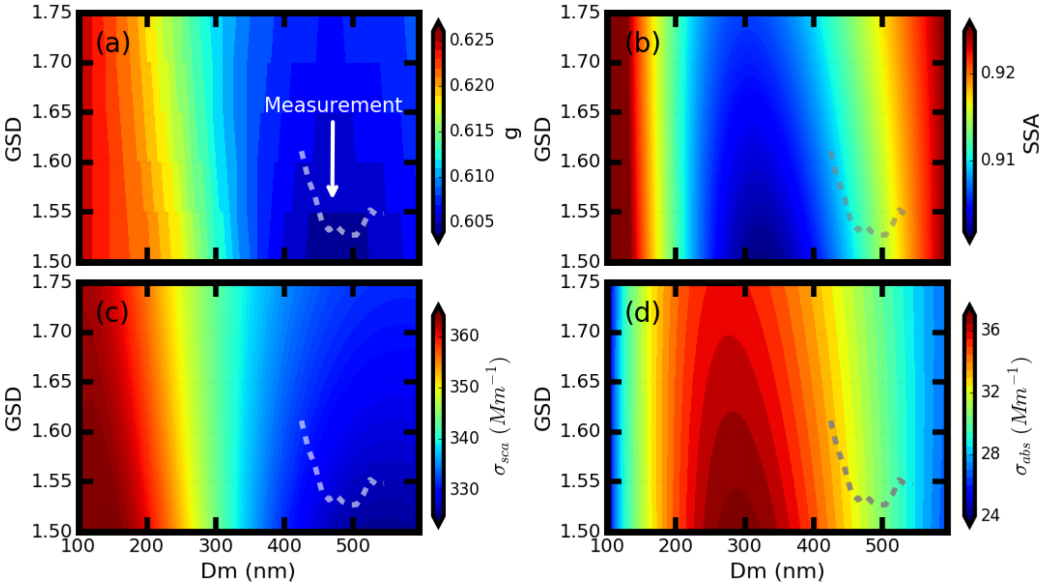

Figure 6. Variations of aerosol optics properties using the measured mean aerosol PNSD and m_{BC} under different BCMSD conditions, which are represented by different Dm and GSD values: (a) aerosol asymmetry factor, (b) single scatter albedo, (c) scattering coefficient and (d) extinction coefficient . The grey dotted line in the figure shows the evolution path of the BCMSD according to results of field measurements.

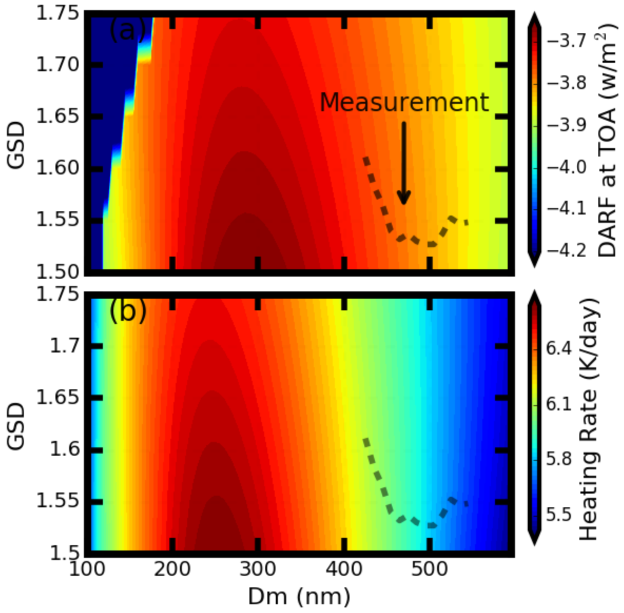

Figure 7. Variations of (a) DARF and (b) heating rate under different BCMSD conditions, which are represented by different Dm and GSD values. The black dotted line in the figure shows the evolution path of the BCMSD according to results of field measurements.

Table 1. Comparison of the DARF and heating rate values under different BC mixing states and different BCMSD conditions.

		Mixing State			BCMSD	
		Internal	External	Core-Shell	Minimum	Maximum
DARF	Value(w/m^2)	-3.45	-3.56	-3.81	-3.97	-3.67
	Variation	10.5%			8.45%	
Heat Rate	Value(K/day)	2.51	2.32	2.53	2.24	2.50
	Variation	9.71%			11.6%	